

Magnetic fields and cosmic rays in M 31 [★]

I. Spectral indices, scale lengths, Faraday rotation, and magnetic field pattern

R. Beck, & E.M. Berkhuisen, R. Gießübel ^{**}, and D.D. Mulcahy ^{***}

Max-Planck-Institut für Radioastronomie, Auf dem Hügel 69, 53121 Bonn, Germany
e-mail: rbeck@mpi.fr-bonn.mpg.de

Received 8 August 2019; accepted 16 October 2019

ABSTRACT

Context. Magnetic fields play an important role in the dynamics and evolution of galaxies; however, the amplification and ordering of the initial seed fields are not fully understood. The nearby spiral galaxy M 31 is an ideal laboratory for extensive studies of magnetic fields.

Aims. Our aim was to measure the intrinsic structure of the magnetic fields in M 31 and compare them with dynamo models of field amplification.

Methods. The intensity of polarized synchrotron emission and its orientation are used to measure the orientations of the magnetic field components in the plane of the sky. The Faraday rotation measure gives information about the field components along the line of sight. With the Effelsberg 100-m telescope three deep radio continuum surveys of the Andromeda galaxy, M 31, were performed at 2.645, 4.85, and 8.35 GHz (wavelengths of 11.3, 6.2, and 3.6 cm). The $\lambda 3.6$ cm survey is the first radio survey of M 31 at such small wavelengths. Maps of the Faraday rotation measures (*RM*s) are calculated from the distributions of the polarization angle.

Results. At all wavelengths the total and polarized emission is concentrated in a ring-like structure of about 7–13 kpc in radius from the centre. Propagation of cosmic rays away from the star-forming regions is evident. The ring of synchrotron emission is wider than the ring of the thermal radio emission, and the radial scale length of synchrotron emission is larger than that of thermal emission. The polarized intensity from the ring in the plane of the sky varies double-periodically with azimuthal angle, indicating that the ordered magnetic field is oriented almost along the ring, with a pitch angle of $-14^\circ \pm 2^\circ$ at $\lambda 6.2$ cm. The *RM* varies systematically along the ring. The analysis shows a large-scale sinusoidal variation with azimuthal angle, signature of an axisymmetric spiral (*ASS*) regular magnetic field, plus a superimposed double-periodic variation of a bisymmetric spiral (*BSS*) regular field with about six times smaller amplitude. The *RM* amplitude of (118 ± 3) rad m⁻² between $\lambda 6.2$ cm and $\lambda 3.6$ cm is about 50% larger than between $\lambda 11.3$ cm and $\lambda 6.2$ cm, indicating that Faraday depolarization at $\lambda 11.3$ cm is stronger (i.e. with a larger Faraday thickness) than at $\lambda 6.2$ cm and $\lambda 3.6$ cm. The phase of the sinusoidal *RM* variation of $-7^\circ \pm 1^\circ$ is interpreted as the average spiral pitch angle of the regular field. The average pitch angle of the ordered field, as derived from the intrinsic orientation of the polarized emission (corrected for Faraday rotation), is significantly smaller: $-26^\circ \pm 3^\circ$.

Conclusions. The dominating axisymmetric (*ASS*) plus the weaker bisymmetric (*BSS*) field of M 31 is the most compelling case so far of a field generated by the action of a mean-field dynamo. The difference in pitch angle of the regular and the ordered fields indicates that the ordered field contains a significant fraction of an anisotropic turbulent field that has a different pattern than the regular (*ASS* + *BSS*) magnetic field.

Key words. Galaxies: spiral – galaxies: magnetic fields – galaxies: ISM – galaxies: individual: M 31 – radio continuum: galaxies – radio continuum: ISM

1. Introduction

Interstellar magnetic fields play an important role in the structure and evolution of galaxies. They provide support to the gas against the gravitational field (Boulares & Cox 1990), affect the star formation rate (Krumholz & Federrath 2019) and the multi-phase structure of the ISM (Evirgen et al. 2019), regulate galactic outflows and winds (Evirgen et al. 2019), and control the propagation of cosmic rays (e.g. Zweibel 2013).

Magnetic fields can be turbulent, ordered, or regular, and are generated by different physical processes. Turbulent fields are amplified by turbulent gas motions, called the small-scale dynamo (e.g. Brandenburg & Subramanian 2005). Ordered fields,

obtained from turbulent fields by compressing and shearing gas flows, reverse their sign on small scales and are called anisotropic turbulent fields. On the other hand, ordered fields generated by the mean-field α - Ω dynamo (Ruzmaikin et al. 1988; Beck et al. 1996; Chamandy 2016) reveal a coherent direction over several kpc and are called regular fields or mean fields (for a review see Beck 2015).

Synchrotron radio emission is the best tool for studying magnetic fields in 3D without effects due to absorption. Synchrotron intensity is a measure of the strength of the field components on the sky plane and the density of cosmic-ray electrons. Linearly polarized synchrotron emission is a signature of the strength and orientation of ordered fields in the plane of the sky. Faraday rotation of the polarization angle increases with the square of the wavelength, the density of thermal electrons, and the strength of regular fields along the line of sight; the sign of the Faraday rotation gives the field direction. Unpolarized synchrotron emis-

[★] Based on observations with the 100-m telescope of the Max-Planck-Institut für Radioastronomie at Effelsberg.

^{**} Present e-mail address: r.giessuebel@gmx.de

^{***} Present e-mail address: david.dec.mulcahy@gmail.com

Table 1. Basic parameters of M 31 \equiv NGC 224.

RA [J2000]	00h 42m 46.1s
DEC [J2000]	+41° 16' 12''
Distance [kpc]	780 \pm 40 ¹
Inclination [°]	75 ²
PA [°]	37 ²
v_{sys} [km s ⁻¹]	-305 \pm 7 ³
v_{rot} [km s ⁻¹] (disc)	230–275 ³
Approaching side	south-west
Receding side	north-east
SFR [M_{\odot} yr ⁻¹]	0.3 ⁴
Classification	SAS3 ⁵

References:

- 1 Stanek & Garnavich (1998)
- 2 Berkhuijsen (1977); Chemin et al. (2009)
- 3 Chemin et al. (2009)
- 4 Tabatabaei & Berkhuijsen (2010); Rahmani et al. (2016)
- 5 de Vaucouleurs et al. (1976)

sion traces turbulent fields (or ordered fields tangled by turbulent gas motions) that cannot be resolved by the telescope beam. Turbulent or tangled fields are strongest in star-forming regions in the gaseous arms of spiral galaxies (Beck 2007; Tabatabaei et al. 2013b) with energy densities similar to that of the turbulent kinetic energy of the gas (Beck 2015). Ordered fields reveal spiral patterns in most galaxies observed so far. Measuring the azimuthal variation of Faraday rotation can reveal large-scale modes of the regular field that are generated by the mean-field dynamo (Krause 1990).

The Andromeda galaxy, M 31, is particularly suited to investigating interstellar magnetic fields thanks to its proximity and prominent ‘ring’ of star formation. The radio emission and magnetic field properties of M 31 have been studied extensively with the Effelsberg 100-m, the Very Large Array (VLA), and the Westerbork Synthesis Radio Telescope (WSRT) (Berkhuijsen 1977; Berkhuijsen et al. 1983; Beck et al. 1980; Beck 1982; Beck et al. 1989, 1998; Berkhuijsen et al. 2003; Gießübel et al. 2013; Gießübel & Beck 2014). The total and polarized emissions are concentrated in a ring-like structure with a radius of about 7–13 kpc from the centre, the region with the highest density of cold molecular gas (Nielen et al. 2006), warm neutral gas (Brinks & Shane 1984; Braun et al. 2009; Chemin et al. 2009), warm ionized gas (Devereux et al. 1994), and dust (Gordon et al. 2006; Fritz et al. 2012); it is the main location of present-day star formation (e.g. Tabatabaei & Berkhuijsen 2010; Rahmani et al. 2016, and references therein).

The first radio polarization survey of M 31 was performed with the Effelsberg telescope at 2.7 GHz (λ 11.1 cm) (Beck et al. 1980). Faraday rotation measures were estimated from the differences between the orientations of the observed polarization vectors and those of a regular field with a constant direction along the azimuthal and radial directions in the emission ring (Sofue & Takano 1981; Beck 1982). The angle differences showed a clear sinusoidal variation with azimuthal angle. This result, as well as the double-periodic azimuthal variation of polarized intensity, were found to be consistent with the ring-like field (Beck 1982). The phase shift of the angle differences relative to the major axis indicated that the field pattern is not a ring, but a tightly wound spiral with a pitch angle of about -10° (Ruzmaikin et al. 1990).¹

¹ A negative pitch angle indicates that the spiral pattern is trailing with respect to the global rotation.

These authors interpreted this regular axisymmetric field with a spiral pattern (ASS) as the lowest mode excited by a large-scale (α - Ω) dynamo. Indication of a superposition of the next higher mode with a lower amplitude, the bisymmetric spiral field (BSF), was found by Sofue & Beck (1987) and Ruzmaikin et al. (1990). However, the above results were based on observations at one single frequency, and thus had to rely on the assumption of a simple field geometry.

Completion of a polarization survey of M 31 at λ 6.2 cm observed with the Effelsberg telescope enabled the calculation of Faraday rotation measures (RMs) between λ 6.2 cm and the previously obtained λ 11.1 cm data, which confirmed the ASS field pattern (Berkhuijsen et al. 2003). Combined with another polarization survey at λ 20.5 cm observed with the Very Large Array (VLA) D-array and the Effelsberg telescope (Beck et al. 1998), a detailed model of the magnetic field was constructed by Fletcher et al. (2004). The spiral pitch angles were found to vary radially from -19° around 9 kpc radius to -8° around 13 kpc radius. The radial field component is directed **inwards** everywhere. Only the mean-field α - Ω dynamo (hereafter referred to as mean-field dynamo) is able to generate a large-scale spiral field that is coherent over the whole galaxy (Beck et al. 1996).

Measurements of the Faraday rotation of the polarized emission from 21 background sources at 1.365 GHz and 1.652 GHz with the VLA B-array gave further support to the ASS field pattern and indicated that this regular field may extend to even 25 kpc radius (Han et al. 1998), but more sources are needed for a statistically safe result (Stepanov et al. 2008).

The central region of M 31, which has an inclination of about 43° (Melchior & Combes 2011), was observed by Gießübel & Beck (2014) at 4.86 GHz and 8.46 GHz with the VLA D-array and was combined with Effelsberg data at similar frequencies. These authors detected a regular field within 0.5 kpc radius that is different from that in the disc. It also reveals an ASS pattern, but the magnetic pitch angle of about -33° is much larger than that of the disc field, and its radial field component is directed **outwards**, opposite to that in the disc. The central region is known to be physically decoupled from the disc (e.g. Jacoby et al. 1985), with a different inclination.

Numerical models of evolving dynamos (e.g. Hanasz et al. 2009; Moss et al. 2012) demonstrated how the field coherence scale grows with galaxy age. Large-scale field reversals may still exist in present-day galaxies if the dynamo is slow or disturbed by gravitational interactions, while some galaxies like M 31 have reached full coherence (Arshakian et al. 2009), except for the central region that probably drives an independently operating mean-field dynamo.

Polarized emission from strongly inclined galaxies like M 31 at wavelengths above about λ 6 cm is diminished by Faraday depolarization along the line of sight through the disc by a magneto-ionic medium (Sokoloff et al. 1998). Faraday depolarization increases strongly with increasing wavelength. In order to reduce depolarization, observations at high frequencies are desired, which also provide higher angular resolution. Furthermore, the extension of magnetic fields into the outer disc of M 31 and a potential radio halo should be investigated by surveys with higher sensitivity. As synchrotron intensity decreases with decreasing wavelength, the range λ 3 cm–6 cm is optimal to observe polarized synchrotron emission from galaxy discs and spiral arms (Arshakian & Beck 2011).

This paper presents three new radio continuum surveys of M 31 with improved sensitivity performed with the Effelsberg 100-m telescope at central frequencies of 2.645, 4.85, and 8.35 GHz (λ 11.33 cm, λ 6.18 cm, and λ 3.59 cm). The surveys at

Table 2. New radio continuum surveys conducted with the Effelsberg 100-m telescope.

Central freq. [GHz]	Bandwidth [MHz]	Wavelength [cm]	HPBW ¹ [']	Map size [']	rms noise (I) ² [mJy/beam]	rms noise (PI) ³ [mJy/beam]	Obs. dates
2.645	70	11.33	4.4	196 x 92	1.2	0.4	Oct 2010
4.85	300	6.18	2.6	140 x 80	0.3	0.05	June 2001–Aug 2005
8.35	1100	3.59	1.4	116 x 40	0.25–0.3 ⁴	0.06–0.12 ⁴	Dec 2001–Sept 2012

Notes:

1 Half-power beamwidth

 2 Noise in total power (I) has an uncertainty of about 20–30% because of residual scanning effects. Noise in I is generally larger than that in polarized intensity (PI) due to confusion by many weak unpolarized background sources.

 3 Noise in PI has an uncertainty of about 10%. Noise in Stokes Q and U is very similar to that in PI .

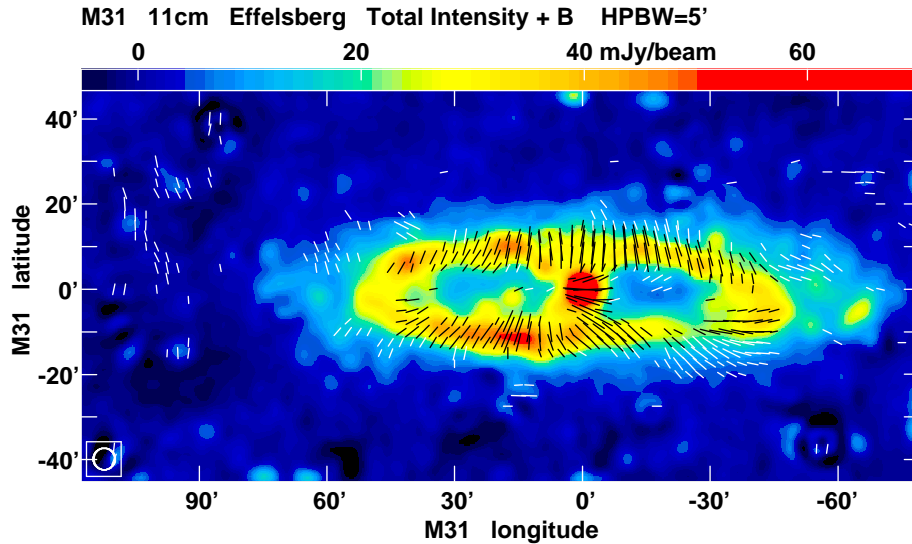
 4 The lower value refers to the noise in the inner part of the map ($40' \times 40'$).


Fig. 1. Total intensity I (in colour) of M 31 at $\lambda 11.3$ cm smoothed to $5'$ HPBW, in coordinates along the major and minor axes of the ring of M 31. The rms noise is 1.0 mJy/beam. The lines show the apparent magnetic field orientations (not corrected for Faraday rotation) at the same resolution with lengths proportional to polarized intensity PI , where the length of a beam width corresponds to 3 mJy/beam. No lines are plotted where PI is below 1.0 mJy/beam or where I is negative. Background sources have been subtracted. The HPBW is indicated in the bottom left corner.

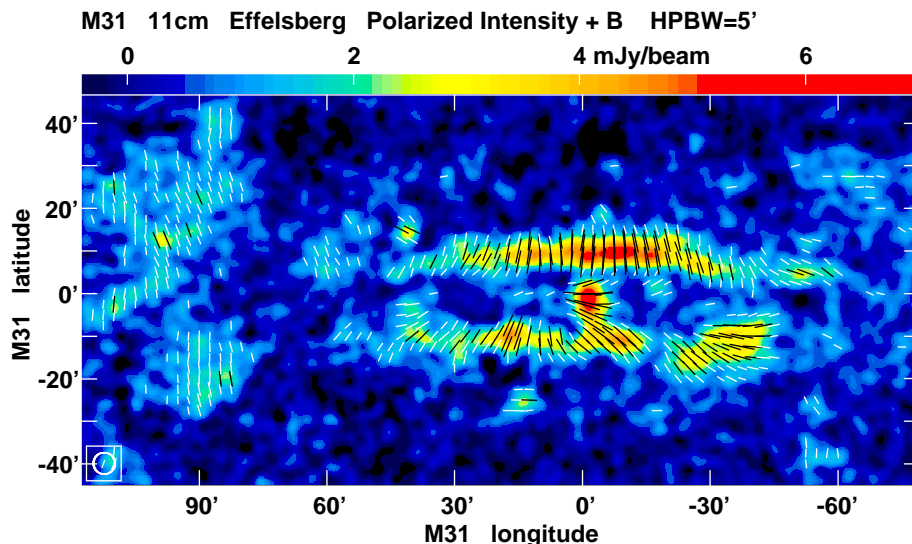


Fig. 2. Polarized intensity PI (in colour) of M 31 at $\lambda 11.3$ cm smoothed to $5'$ HPBW, in coordinates along the major and minor axes of M 31. The rms noise is 0.3 mJy/beam. The lines show the apparent magnetic field orientations (not corrected for Faraday rotation) at the same resolution with lengths proportional to polarized intensity PI , where the length of a beam width corresponds to 3 mJy/beam. No lines are plotted where PI is below 1.0 mJy/beam. Polarized background sources have been subtracted. The HPBW is indicated in the bottom left corner.

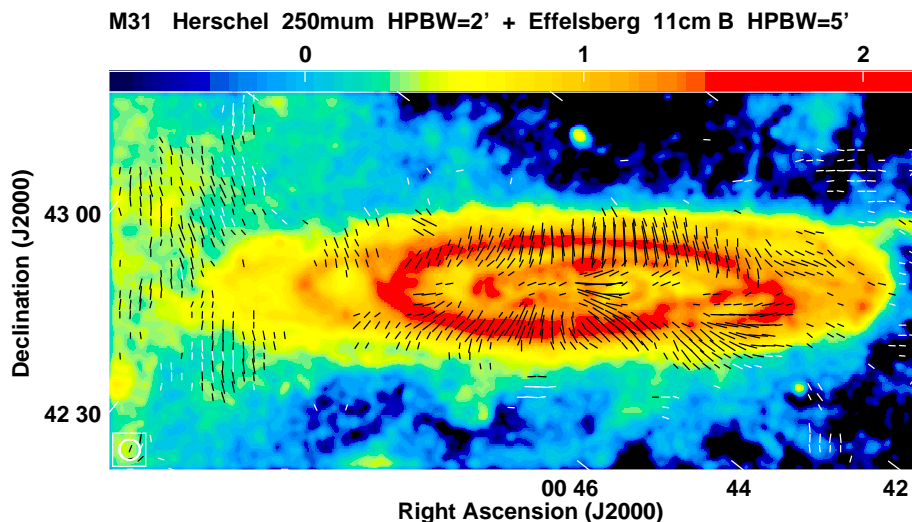


Fig. 3. Apparent magnetic field orientations (not corrected for Faraday rotation) of M 31 at $\lambda 11.3$ cm at $5'$ HPBW with lengths proportional to polarized intensity PI , overlaid onto an image of $250\ \mu\text{m}$ infrared emission from Fritz et al. (2012) (arbitrary units, in \log_{10} scale), smoothed to $2'$ HPBW, indicated in the bottom left corner. The coordinate system is rotated by -53° .

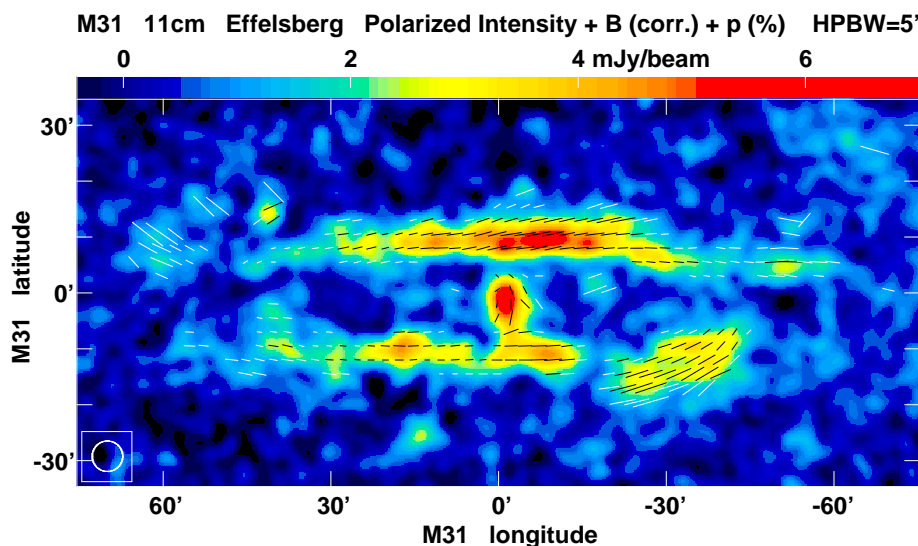


Fig. 4. Polarized intensity PI (in colour) of M 31 at $\lambda 11.3$ cm smoothed to $5'$ HPBW, in coordinates along the major and minor axes of M 31. The rms noise is 0.3 mJy/beam. The lines show the **intrinsic** magnetic field orientations at the same resolution, corrected for Faraday rotation measured between $\lambda 11.3$ cm and $\lambda 6.2$ cm (see Fig. 21), with lengths proportional to the degree of polarization, where the length of a beam width corresponds to 30%. No lines are plotted where I or PI is below 3 times the rms noise. Polarized background sources have been subtracted. The HPBW is indicated in the bottom left corner.

$\lambda 11.3$ cm and $\lambda 6.2$ cm cover larger fields around M 31 than the previous surveys and are also significantly deeper (lower rms noise), especially in polarized intensity where the rms noise is not limited by confusion from weak background sources. Our survey at $\lambda 3.6$ cm is the first one of M 31 at such small wavelengths that covers the entire galaxy.

Section 2 summarizes the observations and data reduction. Section 3 describes the final maps, Sect. 4 the integrated spectrum and the spectral index distributions, Sect. 5 the radial scale lengths of the emission components, Sect. 6 the azimuthal variation of polarized intensity, and Sect. 7 the Faraday rotation measures and the large-scale field pattern. Further analysis concerning magnetic field strengths, depolarization effects, and propagation of cosmic rays will follow in a subsequent paper.

2. Observations and data reduction

2.1. The Effelsberg survey at $\lambda 11.3$ cm

At $\lambda 11.3$ cm, M 31 was observed with the single-horn secondary-focus system of the Effelsberg 100-m telescope. The system backend splits the total bandwidth of 80 MHz into eight channels from 2.60 GHz to 2.68 GHz. The first channel (at the lowest frequency) was affected by strong radio frequency interference (RFI) and could not be used. The central frequency of the remaining channels is 2.645 GHz ($\lambda 11.3$ cm). The receiver outputs are circularly polarized signals that are transformed into signals of Stokes I , Q , and U .

Maps of $196' \times 92'$ were scanned in a coordinate system with the horizontal axis oriented along the major axis of M 31 at a position angle of 37° . Thirty-four coverages in eight observation

sessions were scanned alternating along the directions parallel to the major axis l and the minor axis b of the ring of M 31. All maps were offset by $20'$ along the major axis towards the north-east in order to include the region of the northern spiral arm located at about $110'$ from the centre (Berkhuijsen 1977). One coverage took about 2 h of observation time.

At least one of the polarized quasar radio sources, 3C138 and 3C286, was observed in each observation session for calibration of flux density and polarization angle. Reference values for flux densities were taken from the VLA Calibrator Manual (Perley & Taylor 2003) and from Peng et al. (2000), those for polarization angle from Perley & Butler (2013). The calibration factors, averaged for these two sources, were determined for each channel separately (for details see Mulcahy 2011). The instrumental polarization of the Effelsberg telescope emerges from the polarized sidelobes with 0.3–0.5% of the peak total intensity at the frequencies of the observations presented in this paper and is lower than the rms noise in our maps.

Data processing was performed with the NOD3 software package (Müller et al. 2017b). Four of the 34 coverages could not be used because of strong scanning effects due to bad weather conditions. In the remaining coverages, regions with RFI were blanked by hand. The remaining coverages, separated into maps scanned in l and in b , were averaged with a median filter. The resulting maps, two each in I , Q , and U , were combined in the image plane with the Mweave option. This ‘basket-weaving’ technique reduces the scanning effects in the coverages. It was originally developed by Chris Salter (see Sieber et al. 1979).

The resulting maps in Q and U were combined into a map of polarized intensity (PI) and polarization angle with the PolInt option that includes a correction for positive bias due to noise and ensures that the PI map has the same (Gaussian) noise statistics as the maps in Q and U (Müller et al. 2017a). Hence, we give only the noise values for PI in Table 2.

As we are interested in the diffuse emission from M 31, we subtracted 56 unresolved background sources above the flux density level of 10 mJy in total intensity (I) with the Gaus2 option of NOD2. In polarized intensity (PI), five background sources above five times the rms noise level were detected and subtracted. Lastly, we smoothed all the final maps from the original resolution of 4.4 HPBW to $5'$ HPBW in order to increase the signal-to-noise ratio. The rms noise in the 4.4 image in I is about two times lower than that in the previous image at a similar frequency (Beck et al. 1980), while the improvement in PI is about a factor of three.

The plots of the final maps were performed with the AIPS software package.

2.2. The Effelsberg survey at $\lambda 6.2$ cm

At $\lambda 6.2$ cm, M 31 was observed with the two-horn secondary-focus system of the Effelsberg 100-m telescope. The system backend records signal in a single band of 500 MHz width, with a central frequency of 4.85 GHz ($\lambda 6.2$ cm). The receiver outputs are circularly polarized signals that are transformed into signals of Stokes I , Q , and U in a digital correlator.

Maps of $140' \times 80'$, centred on the nucleus of M31, were scanned in the coordinate system oriented along the major axis. A total of 101 coverages in 20 observation sessions were scanned alternating along the directions parallel to the major axis l and the minor axis b . One coverage took about 2 h of observation time. At least one of the calibration sources, 3C138 or 3C286, was observed in each observation session.

Thirty of the 101 coverages could not be used because of strong scanning effects due to bad weather conditions. In the remaining coverages, regions with RFI were blanked by hand. Data reduction was performed with the NOD2 and NOD3 software packages. Each coverage gave maps in Stokes I , Q , and U from each of the two horns that are separated by 8.1 in azimuthal angle on the sky. The dual-beam restoration technique to reduce effects of weather (Emerson et al. 1979; Müller et al. 2017b) could not be applied because scanning was done in the coordinate system of M 31 to save observation time. Hence, the coverage from the second horn was shifted by applying the script subtrans (described in Kothes et al. 2017) and added to the coverage from the first horn. The coverages were combined applying the turboplait script based on a Fourier transform (following Emerson & Gräve 1988) that reduces the scanning effects by optimizing the base levels of the orthogonally scanned coverages. All coverages were treated by applying the NOD2 script fchop that removes the signals at spatial frequencies that correspond to baselines larger than the telescope size of 100 m. This slightly reduced the final angular resolution from 2.45 to 2.6 HPBW.

At $\lambda 6.2$ cm, we subtracted 28 unresolved background sources above the flux density level of 6 mJy in I . In PI , 14 background sources above 10 times the rms noise level were subtracted. Lastly, we smoothed the final maps to $3'$ HPBW in order to increase the signal-to-noise ratio. The rms noise in the 2.6 image in I is about 1.5 times lower than that in the previous image at the same frequency (Berkhuijsen et al. 2003), while the improvement in PI is a factor of about 2.5.

2.3. The Effelsberg survey at $\lambda 3.6$ cm

At $\lambda 3.6$ cm, M 31 was observed with the single-horn secondary-focus system of the Effelsberg 100-m telescope with a total size of $116' \times 40'$. The system backend records signal in a single band of 1100 MHz width, with a central frequency of 8.35 GHz. The receiver outputs are circularly polarized signals that are transformed into signals of Stokes I , Q , and U in a digital correlator.

The project required a huge effort due to the weak emission of the galaxy at this frequency and the small telescope beam compared to the large angular size of M 31. We started with a small test field of $10' \times 10'$ centred on the galaxy nucleus, taking about 25 min observation time per coverage, followed by two adjacent fields of $25' \times 17'$ to the north-west and south-east and another two fields of $17' \times 25'$ to the north-east and south-west, taking about 1 h observation time per coverage and per field. Overlaps of $2'$ allowed us to adjust the base levels. Between December 2001 and October 2007, about 40 coverages per field were scanned along alternating directions parallel and perpendicular to the major axis (galaxy coordinates l and b). At least one of the two calibration sources, 3C138 or 3C286, was observed in each observation session.

Data reduction was performed with the NOD2 and NOD3 software packages. About 10% of the coverages could not be used because of bad weather conditions. In the remaining coverages, regions with RFI were blanked by hand. The coverages from each field scanned in the l and b directions were averaged separately. Combining the l and b maps from each field of the inner region needed special attention because the diffuse emission is more extended in the l direction than the field size, so that the option turboplait or Mweave could not be applied. The following procedure was performed: (1) In the b map (where strong unresolved sources are subtracted), fit and subtract linear baselines in the l direction; (2) Subtract the resulting b map from

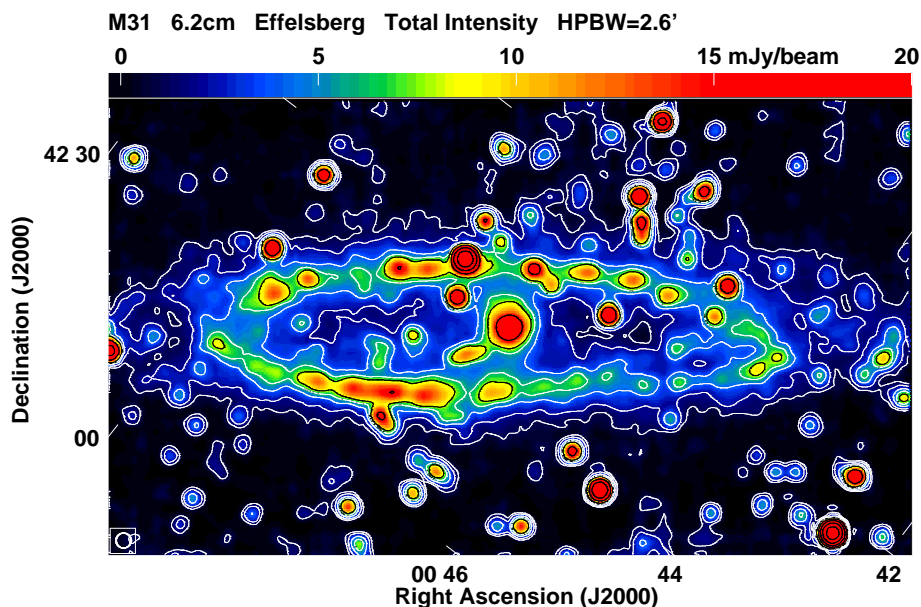


Fig. 5. Total intensity I (colour and contours) of M 31 at $\lambda 6.2$ cm at the original HPBW of $2.6'$. Contour levels are at $(1, 2, 4, 8, 16, 32, 64, 128) \times 1$ mJy/beam. The rms noise is 0.3 mJy/beam. The HPBW is indicated in the bottom left corner. The coordinate system is rotated by -53° .

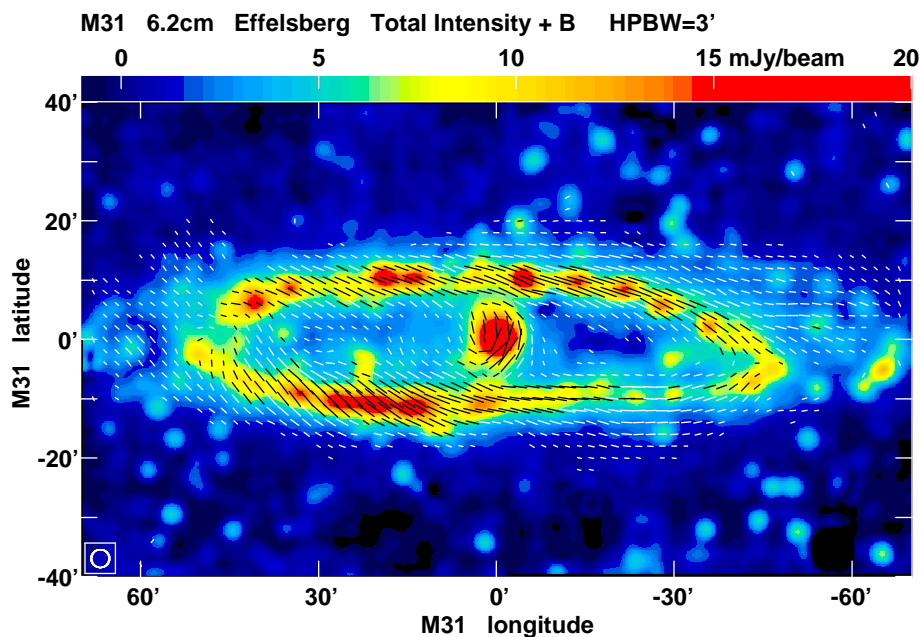


Fig. 6. Total intensity I (in colour) of M 31 at $\lambda 6.2$ cm smoothed to $3'$ HPBW, in coordinates along the major and minor axes of M 31. The rms noise is 0.35 mJy/beam. The lines show the apparent magnetic field orientations (not corrected for Faraday rotation) at the same resolution with lengths proportional to polarized intensity PI , where the length of a beam width corresponds to 1.5 mJy/beam. No lines are plotted where PI is below 0.3 mJy/beam or where I is negative. Background sources have been subtracted. The HPBW is indicated in the bottom left corner.

the original b map to obtain a map of large-scale structures in the b direction; (3) In the l maps (where again strong unresolved sources are subtracted), fit and subtract linear baselines in the l direction; (4) Subtract the resulting l map from the original l map to obtain a map of large-scale structures in the l direction; (5) Compute the difference of the maps obtained in steps (2) and (4) to obtain the large-scale emission missing in the l map; (6) Add the result from step (5) to the l map. Details of the data reduction have been described by Gießübel (2012).

The combination of the first five fields yielded a map of $40' \times 40'$ centred on the galaxy nucleus. The high investment in

observation time resulted in a low rms noise of 0.25 mJy/beam in I and 0.06 mJy/beam in PI .

After successful completion of the central part, we decided to extend the survey to cover most of the galaxy disc out to a distance of $l = \pm 58'$ (13.2 kpc) from the centre. This was achieved by observing two fields on both sides of the major axis of $40' \times 40'$ each, overlapping by $2'$ with the central part, taking about 1.7 h of observation time per coverage. Between November 2011 and September 2012, 24 coverages per field were scanned alternating along the horizontal (l) and vertical (b) galaxy coordinates, of which ten could not be used because of

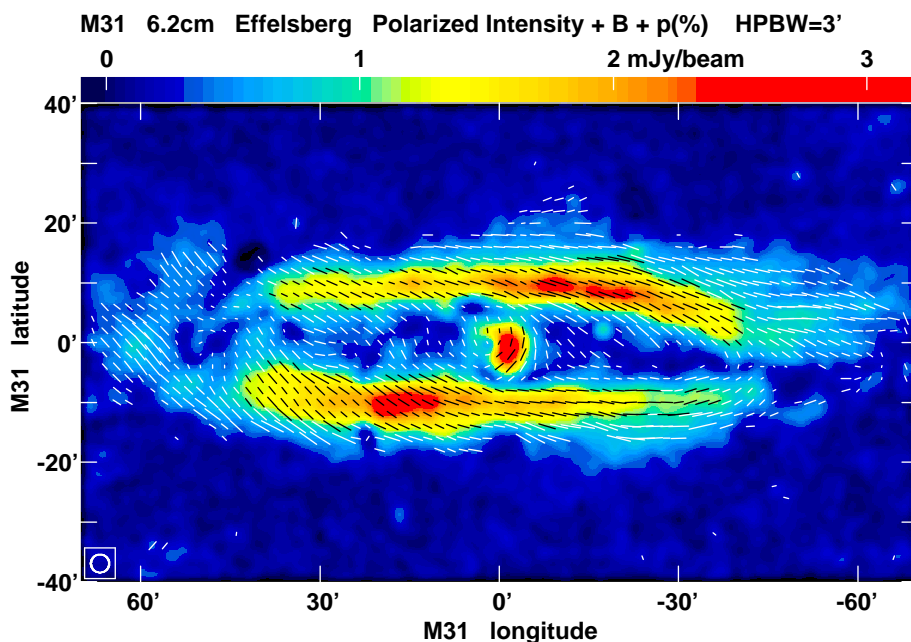


Fig. 7. Polarized intensity PI (in colour) of M 31 at $\lambda 6.2$ cm smoothed to $3'$ HPBW, in coordinates along the major and minor axes of M 31. The rms noise is 0.06 mJy/beam. The lines show the apparent magnetic field orientations (not corrected for Faraday rotation) at the same resolution with lengths proportional to the degree of polarization, where the length of a beam width corresponds to 30%. No lines are plotted where I or PI is below 3 times the rms noise. Polarized background sources have been subtracted. The HPBW is indicated in the bottom left corner.

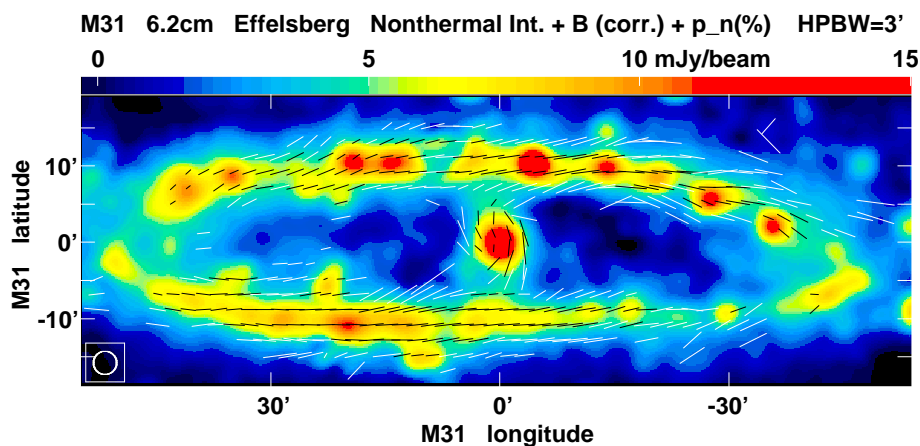


Fig. 8. Total non-thermal intensity (in colour) of M 31 at $\lambda 6.2$ cm smoothed to $3'$ HPBW, in coordinates along the major and minor axes of M 31. The rms noise is 0.35 mJy/beam. The lines show the **intrinsic** magnetic field orientations at the same resolution, corrected for Faraday rotation measured between $\lambda 6.2$ cm and $\lambda 3.6$ cm (see Fig. 22), with lengths proportional to the degree of non-thermal polarization, where the length of a beam width corresponds to 30%. No lines are plotted where PI is below 0.2 mJy/beam. Polarized background sources have been subtracted. The HPBW is indicated in the bottom left corner.

bad weather conditions. The combination of the fields was done by adjusting the base levels in the overlap regions. The seven fields cover a total size of $116' \times 40'$ in the coordinate system of M 31. As the number of coverages of the two outer fields was smaller than for the inner part, the rms noise is higher, i.e. 0.3 mJy/beam in I and 0.12 mJy/beam in PI .

The extent of the final map of $b = \pm 20'$ from the major axis of M 31 (17.5 kpc in the galaxy plane) was chosen to keep the total observation time within a manageable limit, even though we were aware that some of the faint diffuse emission from the outer disc would be missing due to the base level subtraction.

In an attempt to correct for the largest scales of emission, we observed a grid of 11 scans of $70'$ in length perpendicular to

the plane (in b), separated by $4'$ along the plane, and combined them into an undersampled map of $40' \times 70'$. All observations took place before local sidereal time $LST = 00^{\text{h}}40^{\text{m}}$ (i.e. before M 31 crossed the meridian). When the galaxy was rising, its major axis remained approximately parallel to the Earth's horizon. Our scanning speed of $20''/s$ was close to the apparent speed of the sky. When scanning in the negative b direction before $LST = 00^{\text{h}}40^{\text{m}}$, the telescope remained almost still as the sky moved across. The atmospheric and ground emission thus remained more or less constant during a scan. On the other hand, when scanning in the positive b direction, the telescope had to move fast in elevation, almost two times as fast as just tracking M 31, so that the signal was affected by varying atmospheric

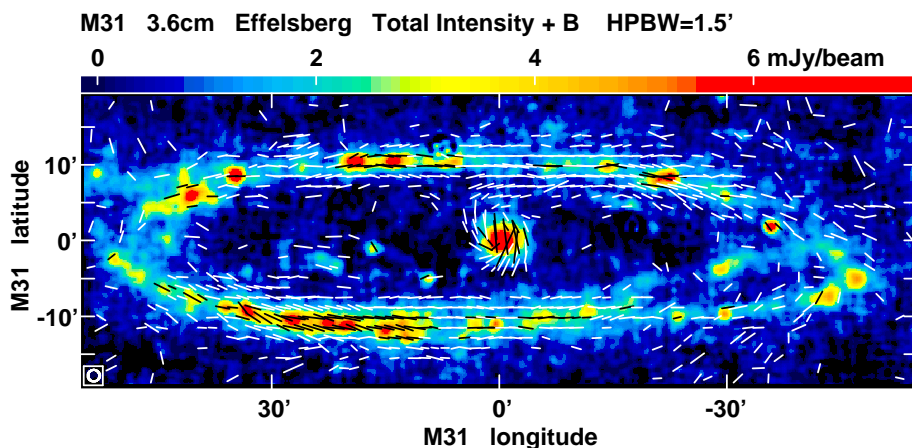


Fig. 9. Total intensity I (colour) of M 31 at $\lambda 3.6$ cm smoothed to $1.5'$ HPBW, in coordinates along the major and minor axes of M 31. The rms noise is 0.25 mJy/beam in the inner part ($40' \times 40'$) and 0.3 mJy/beam in the outer parts. The lines show the apparent magnetic field orientations (not corrected for Faraday rotation) at the same resolution with lengths proportional to polarized intensity PI , where the length of a beam width corresponds to 0.225 mJy/beam. No lines are plotted where PI is below 0.15 mJy/beam or where I is negative. Background sources have been subtracted. The HPBW is indicated in the bottom left corner.

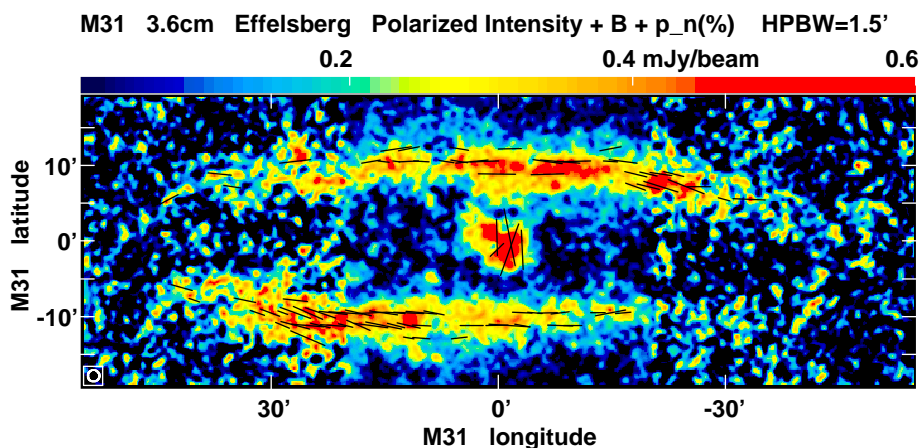


Fig. 10. Polarized intensity PI (colour) of M 31 at $\lambda 3.6$ cm smoothed to $1.5'$ HPBW, in coordinates along the major and minor axes of M 31. The rms noise is 0.045 mJy/beam in the inner part and 0.09 mJy/beam in the outer parts. The lines show the apparent magnetic field orientations (not corrected for Faraday rotation) at the same resolution with lengths proportional to the degree of non-thermal polarization, where the length of a beam width corresponds to 10% . No lines are plotted where I or PI is below 3 times the rms noise. Polarized background sources have been subtracted. The HPBW is indicated in the bottom left corner.

and ground emission. In order to add as little uncertainty to the correction as possible, we decided to use only those scanned in the negative b direction where the effects of the atmospheric and ground emission were negligible.

To ensure well-defined base levels for the correction grid, we observed three additional I scans of $70'$ length crossing the lower ends of the b scans and three scans crossing their upper ends. A comparison with the levels of the b scans with those of the I scans at the intersection points showed that only minor corrections were necessary. This demonstrated that the b scans of the grid were long enough to define correct base levels.

The correction grid was then used to define the base level of each of the five inner fields. The amount of missing flux at the map edges compared to the correction grid was determined by subtracting the average over five pixels in the scanning direction. The $4'$ gap between the correction scans was then interpolated by fitting a polynomial to these data points. The order of the polynomial was chosen to be as small as possible, from first to fourth, depending on which one best described the shape

determined by the grid. The actual baseline correction along the direction of the grid used only a linear fit between the bottom and top to ensure an unbiased correction. Only small and linear additional baseline corrections were applied where necessary so that the individual maps matched up correctly in the overlap region. A more thorough description and comparison of the maps before and after the correction can be found in Gießübel (2012).

At $\lambda 3.6$ cm, we subtracted 38 unresolved background sources above the flux density level of 1.2 mJy in I . In PI , six background sources above five times the rms noise level were detected and subtracted. Lastly, we smoothed the final maps from the original resolution of $1.4'$ to $1.5'$ HPBW in order to increase the signal-to-noise ratios.

3. Final maps

The total radio continuum emission from M 31 (Figures 1, 6, and 9) is concentrated in the well-known ring-like structure between 7 kpc and 13 kpc from the galaxy centre. Strong emission

emerges from regions with high star formation rates ($SFRs$) evident from their $H\alpha$ emission (Devereux et al. 1994), as discussed by Tabatabaei & Berkhuijsen (2010). The spatially resolved radio–far-infrared correlation in galaxies, first found in M 31 (Beck & Golla 1988), was studied in M 31 in detail (Hoernes et al. 1998; Berkhuijsen et al. 2013) and confirmed the close relationship between $SFRs$ and total radio continuum emission. The central region of M 31 is radio-bright in spite of its low SFR, possibly because cosmic-ray electrons are (re-) accelerated by shock fronts responsible for the filamentary $H\alpha$ emission (Jacoby et al. 1985).

Figure 5 shows the full field of the total emission at $\lambda 6.2$ cm before subtraction of the background sources that are unrelated to M 31. These sources have been discussed before by Berkhuijsen et al. (1983).

The linearly polarized emission from M 31 (Figures 2, 7, and 10) is also concentrated in the ring-like structure. The main differences to the distribution of total emission are the minima around the major axis of the projected ring. This shows that the ordered magnetic field in the ring is oriented almost along the line of sight on the major axis, and hence almost follows the ring (Beck 1982). The variation of polarized intensity along the ring is discussed in Section 7.

Significant polarized emission (more than 3 times the rms noise) is detected at $\lambda 11.3$ cm also outside the ring of M 31 in the NE (Fig. 2). Some regions are about the same size as the telescope beam and could be weak polarized background sources. Extended polarized patches may originate in the foreground of our Milky Way. Polarized patches in the region of M 31 were also observed at $\lambda 21.1$ cm (Berkhuijsen et al. 2003). They are called Faraday ghosts, and are caused by Faraday rotation and depolarization of smooth polarized emission occurring in nearby magnetized regions in the foreground. They appear only in PI , but not in total intensity I , and are especially prominent when observing at lower frequencies, for example with the WSRT at around $\lambda 90$ cm (e.g. Haverkorn et al. 2003; Schnitzeler et al. 2009) or around $\lambda 2$ m (150 MHz) (e.g. Iacobelli et al. 2013), or with the Low Frequency Array (LOFAR) at around $\lambda 2$ m (e.g. Jelić et al. 2015; Van Eck et al. 2017). Some of the polarized regions outside of the ring to the north-east may originate in high-velocity $H\text{I}$ clouds belonging to M 31 that are mixed with dust seen at $250\ \mu\text{m}$ (Fritz et al. 2012) (see Fig. 3).

The apparent magnetic field orientations (i.e. the polarization angles $+90^\circ$) in Figs. 1, 6, and 9 strongly differ for the three frequencies, demonstrating the action of Faraday rotation. The orientations of the intrinsic magnetic field (corrected for Faraday rotation) shown in Figures 4 and 8 agree well and show that the magnetic field closely follows the ring. In Sect. 7, maps of Faraday rotation measures are discussed.

The two regions of polarized emission outside the ring towards the north, detected at $\lambda 11.3$ cm and $\lambda 6.2$ cm, allowed us to compute the intrinsic field orientations in these areas (Fig. 4, near the left edge of the plot). These strongly deviate from the orientation of the ring and suggest a location in high-velocity clouds around M 31 or in the Milky Way foreground.

4. Spectral index

4.1. Spectral index of the integrated flux density

The galaxy M 31 has been mapped in radio continuum at more than six frequencies (see Table 3). In order to subtract the same point sources from all maps, the flux densities of the sources subtracted at 408 MHz were scaled to the frequencies of the other

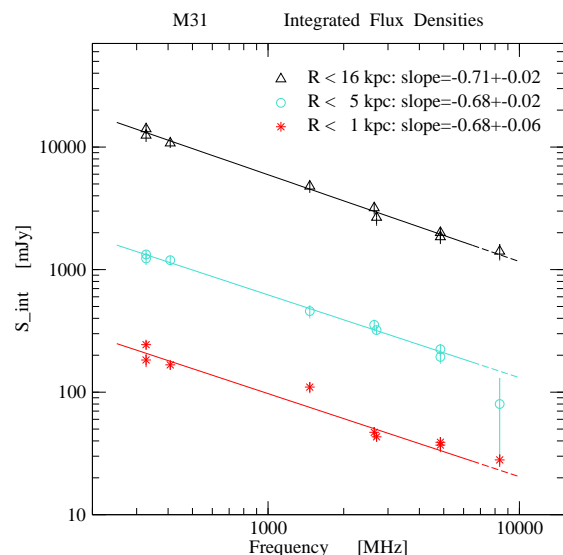


Fig. 11. Spectrum of the integrated flux density of total intensity I integrated to radii of 1 kpc (red), 5 kpc (cyan), and 16 kpc (black). The slopes of the fitted lines are also given in the figure. The points at $\lambda 3.6$ cm were not used for the fits.

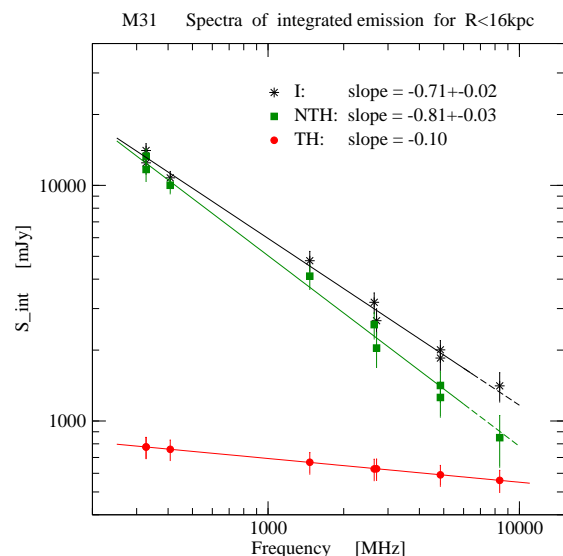


Fig. 12. Spectrum of the integrated flux densities of total intensity I (black), non-thermal intensity NTH (green), and thermal intensity TH (red), integrated to a radius of 16 kpc. The slopes of the fitted lines are also given in the figure. The uncertain points for I and NTH at $\lambda 3.6$ cm were not used for the fits. The points for TH were scaled from the thermal map at $\lambda 20.5$ cm using a slope of -0.1 .

maps, assuming a constant spectral index of $\alpha = 0.7$ (where $S \propto \nu^{-\alpha}$). These flux densities are indicated by S_{\min} in Table 3. After subtracting sources with flux densities $S > S_{\min}$, we used the data to calculate the total spectral index α of the emission integrated in three radial intervals in M 31 (i.e. $R < 1$ kpc, $R < 5$ kpc and $R < 16$ kpc).

Not all maps extend to $R = 16$ kpc ($= 70'$) along the major axis. By comparing them to larger maps we estimated that in these cases about 5% of the flux density was missing and we corrected for this.

The base levels of the maps are usually set to zero in strips that are a few beam widths wide and parallel to the major axis at

Table 3. Integrated flux densities of M 31 for three radial ranges for total intensity I , non-thermal intensity NTH , and thermal intensity TH .

Freq. [MHz]	S_{\min} [mJy] ¹	$R < 1$ kpc I [mJy]	$R < 5$ kpc I [mJy]	$R < 16$ kpc I [mJy]	$R < 16$ kpc TH [mJy] ²	$R < 16$ kpc NTH [mJy]	Reference
327	47	244 ± 18	1320 ± 100	14070 ± 1030 ³	775 ± 80	13290 ± 1040	Golla (1989)
327	47	183 ± 18	1230 ± 120	12470 ± 1250	775 ± 80	11690 ± 1250	Gießübel (2012)
408	40	167 ± 12	1190 ± 90	10770 ± 750	760 ± 75	10010 ± 760	Beck & Gräve (1982)
1465	15	110 ± 10	460 ± 50	4790 ± 480	670 ± 70	4120 ± 490	Beck et al. (1998)
2645	10	47 ± 5	354 ± 35	3190 ± 320	625 ± 65	2570 ± 330	This paper
2702	10	43 ± 2	321 ± 22	2670 ± 340	625 ± 65	2040 ± 350	Beck et al. (1980)
4850	6	39 ± 4	194 ± 22	1850 ± 210 ⁴	590 ± 60	1260 ± 220	Berkhuijsen et al. (2003)
4850	6	37 ± 4	224 ± 22	2010 ± 200	590 ± 60	1420 ± 210	This paper
8350	4	28 ± 3	80 ± 50	1410 ± 200 ⁵	560 ± 60	850 ± 210	This paper

Notes: ¹ Minimum flux density of subtracted sources (see text for details); ² thermal flux densities are based on the thermal map at $\lambda 20.5$ cm of Tabatabaei et al. (2013a), increased by 5% for missing areas near the major axis at $R > 13$ kpc; ³ corrected for missing spacings; ⁴ corrected for missing areas near the major axis at $R > 13$ kpc; ⁵ increased by 5% for missing areas near the major axis at $R > 13$ kpc.

$|b| \approx 30'$. Only the new map at $\lambda 3.6$ cm does not reach that far. Therefore, we adjusted this map to the background level of the new map at $\lambda 6.2$ cm at $|b| \approx 20'$ (after smoothing it to HPBW = $3'$) using the task `bascor` of the NOD2 system. For this adjustment we assumed $\alpha = 0.9$ between $\lambda 6.2$ cm and $\lambda 3.6$ cm at $|b| \approx 20'$. This resulted in an increase in the integrated flux density for $R < 16$ kpc of 200 mJy.

The integration was done by adding the emission in circular rings around the centre in the plane of the galaxy. The resulting flux densities in total power of the three radial intervals are given in Table 3 and are shown in Figure 11. The low value at $\lambda 3.6$ cm for $R < 5$ kpc indicates that, in spite of the great efforts (Section 2.3), the subtracted base level of the small map around the central region was still too high.

Because of the uncertainty in the flux densities at $\lambda 3.6$ cm, we calculated the spectral index between $\lambda 92$ cm (0.327 GHz) and $\lambda 6.2$ cm (4.85 GHz) yielding $\alpha = 0.68 \pm 0.06$ for $R < 1$ kpc, $\alpha = 0.68 \pm 0.02$ for $R < 5$ kpc, and $\alpha = 0.71 \pm 0.02$ for $R < 16$ kpc. Berkhuijsen et al. (2003) found $\alpha = 0.83 \pm 0.13$ for $R < 16$ kpc using only data at $\lambda 20.5$ cm and $\lambda 6.2$ cm. Within the errors their value is consistent with our value, but since our value is based on more data points and a larger frequency interval, our value of $\alpha = 0.71 \pm 0.02$ supersedes the old one.

In order to derive the non-thermal spectral index of the emission integrated to $R < 16$ kpc, we subtracted the integrated thermal emission from the total emission at each frequency, scaled from the integrated thermal emission at $\lambda 20.5$ cm given by Tabatabaei et al. (2013b), using the spectral index of optically thin free-free emission of 0.1. Before scaling, we increased the value at $\lambda 20.5$ cm by 5% to account for missing areas in the thermal map near the major axis. Figure 12 shows the total, non-thermal, and thermal spectra of the integrated emission. A weighted fit through the non-thermal flux densities between $\lambda 92$ cm and $\lambda 6.2$ cm gives the non-thermal spectral index $\alpha_n = 0.81 \pm 0.03$. This shows that the value of $\alpha_n = 1.0$ between $\lambda 20.5$ cm and $\lambda 6.2$ cm assumed by Berkhuijsen et al. (2003) was too large, and demonstrates that spectral indices measured between only two frequencies do not always agree with that derived by fitting the data at many frequencies.

4.2. Maps of spectral index between $\lambda 20.5$ cm and $\lambda 3.6$ cm

Figure 12 shows that the integrated flux densities for $R < 16$ kpc at $\lambda 3.6$ cm agree with the extensions of the lines fitted through the points at the lower frequencies. This indicates that the base

level of the map at $\lambda 3.6$ cm outside the central area is correct. Therefore, we can calculate spectral index maps between $\lambda 20.5$ cm (Beck et al. 1998) and $\lambda 3.6$ cm of total emission (α) and non-thermal emission (α_n) at the best available angular resolution of $90''$ HPBW.

Before calculating spectral index maps, we subtracted from both maps the same point sources (i.e. all sources with flux densities above 5 mJy at $\lambda 20.5$ cm and above 1.2 mJy at $\lambda 3.6$ cm). In order to obtain maps of non-thermal emission at these frequencies, we subtracted maps of thermal emission from the maps of total emission. We used the thermal map at $\lambda 20.5$ cm that Tabatabaei et al. (2013b) derived from the extinction-corrected $H\alpha$ map of Devereux et al. (1994), which we smoothed to $90''$ HPBW and scaled to $\lambda 3.6$ cm by the factor $(3.6/20.5)^{0.1}$, using the thermal spectral index of 0.1. Both I maps were cut down to the size of the thermal map of $110' \times 39'$ in $l \times b$ before subtracting TH from I , and all maps were transformed onto the same grid. Figure 2 in Tabatabaei et al. (2013b) shows that due to the propagation of cosmic ray electrons (CREs) the distribution of the NTH emission is much more extended than that of the TH emission.

For the spectral index calculation, only data points above two times the noise level in both maps were used. The resulting maps of α and α_n are shown in Figures 13 and 14, respectively. We note that because of the base level problems in the innermost region $10' \times 10'$ in size at $\lambda 3.6$ cm, the spectral indices cannot be trusted there.

In Figure 13, values of α in the ring vary from about 0.4 in the middle of the ring where the H_{II} regions are located to > 1.0 in the outer regions of the ring where most of the emission is NTH . The values of α_n in Figure 14 show the same trend as those of α , but are about 0.1 higher in the H_{II} regions in the middle of the ring, varying between 0.5 here and > 1.0 in the outer regions. A value of $\alpha_n = 0.5$ near star-forming regions indicates that the CREs are still close to their birth places in the supernova remnants. Energy losses during the propagation away from their birth places cause the larger spectral indices in the outer parts of the ring.

In Figures 13 and 14 the spectral indices are larger in the southern half of M 31 (right-hand part) than in the northern half. The α map of (Berkhuijsen et al. 2003) between $\lambda 20.5$ cm and $\lambda 6.2$ cm shows the same trends as seen in Figure 13, but with less detail because of the larger HPBW of $3'$.

Due to the large frequency interval between $\lambda 20.5$ cm and $\lambda 3.6$ cm, the random noise errors in the spectral index maps are

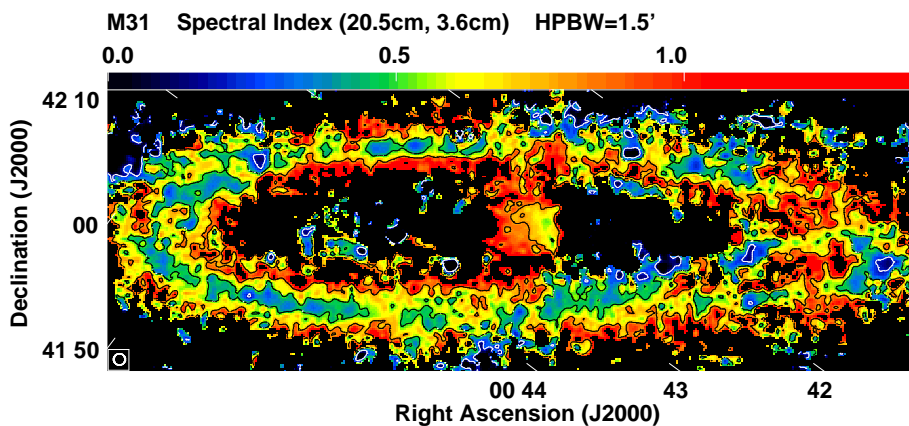


Fig. 13. Spectral index of the total intensity between $\lambda 20.5$ cm and $\lambda 3.6$ cm at $1.5'$ HPBW, calculated at pixels where I at both frequencies exceeds two times the rms noise. Contour levels are at 0.2, 0.5, and 0.8. Background sources have been subtracted. The HPBW is indicated in the bottom left corner. The coordinate system is rotated by -53° .

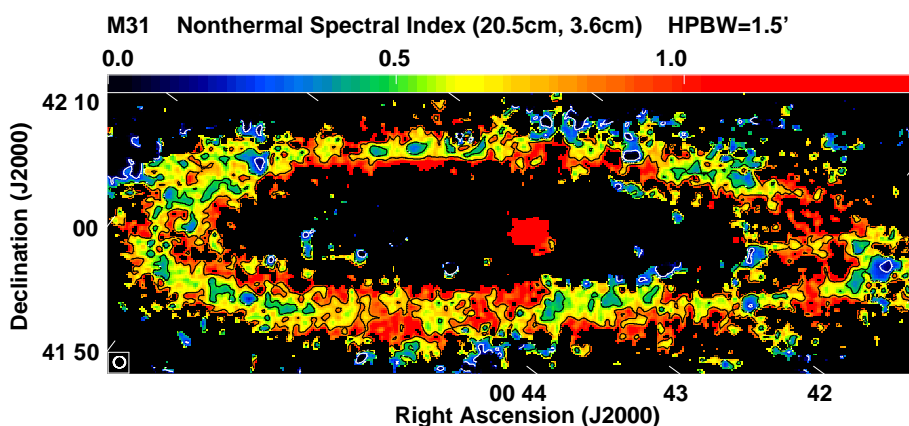


Fig. 14. Spectral index of the non-thermal intensity between $\lambda 20.5$ cm and $\lambda 3.6$ cm at $1.5'$ HPBW, calculated at pixels where I at both frequencies exceeds two times the rms noise. Contour levels are at 0.2, 0.5, and 0.8. Background sources have been subtracted. The HPBW is indicated in the bottom left corner. The coordinate system is rotated by -53° .

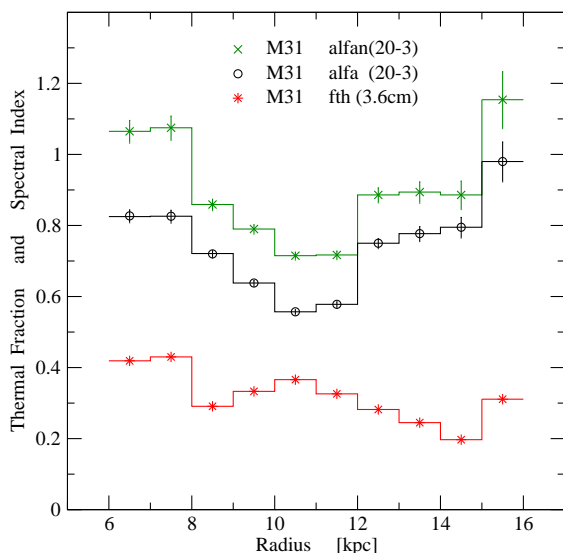


Fig. 15. Radial variations of the spectral index between $\lambda 20.5$ cm and $\lambda 3.6$ cm, of the total intensity (black), of the non-thermal intensity (green), and of the thermal fraction at $\lambda 3.6$ cm (red); they are all at $1.5'$ HPBW.

quite small, ranging from 0.013 in the middle of the ring to 0.038 in the outer parts of the ring in α (Figure 13) and from 0.023 to 0.046 in α_n (Figure 14). The errors are dominated by the noise errors in the maps at $\lambda 3.6$ cm. Systematic errors due to base level uncertainties are difficult to estimate, but could be larger than the random noise errors.

We also calculated spectral index maps between $\lambda 20.5$ cm and $\lambda 6.2$ cm and between $\lambda 6.2$ cm and $\lambda 3.6$ cm at the resolution of $3'$ HPBW. They are consistent with Figures 13 and 14, but because of the larger beam width and the narrower frequency ranges, less interesting than the higher resolution spectral index maps between $\lambda 20.5$ cm and $\lambda 3.6$ cm shown here. The *NTH* map at $\lambda 6.2$ cm is shown in Fig. 8.

4.3. Radial variations in spectral index

In Figure 15 we show the radial variation in α and α_n , and the fraction of thermal emission (f_{th}), averaged in 1 kpc wide rings between $R = 6$ kpc and $R = 16$ kpc. As discussed above, the flattest spectra occur in the middle of the ring ($R = 10 - 11$ kpc) where most of the H_{II} regions are located and the *TH* fraction of the emission is highest. Due to the subtraction of the thermal emission, the spectrum of the *NTH* emission is typically steeper by about 0.1 than that of the total emission I , and both spec-

tra become significantly steeper towards the edges of the emission ring where the *NTH* emission dominates. This suggests that CREs move inwards and outwards away from their birth places near star-forming regions over several kpc in radius.

5. Radial scale lengths

It is interesting to see how the various types of emission from M 31 vary with radial distance to the galaxy centre.

In Figure 16 we show the radial distributions of total emission and polarized emission in the new map at $\lambda 6.2$ cm with angular resolution of 2.6 HPBW. The emissions were averaged in 1 kpc wide circular rings in the plane of M 31 using a constant inclination of 75° . As this map extends $140'$ in longitude, the radial distribution is complete out to $R = 18$ kpc, beyond which some emission near the major axis is missing. The *I* emission from the bright ring peaks at $R = 10 - 11$ kpc and the *PI* emission at 9 kpc, then both emissions steadily decrease to about $R = 20$ kpc. Exponential fits for the range $R = 9 - 20$ kpc yield radial scale lengths of $L = (3.4 \pm 0.2)$ kpc in *I* and $L = (4.43 \pm 0.06)$ kpc in *PI*, as indicated in the figure.

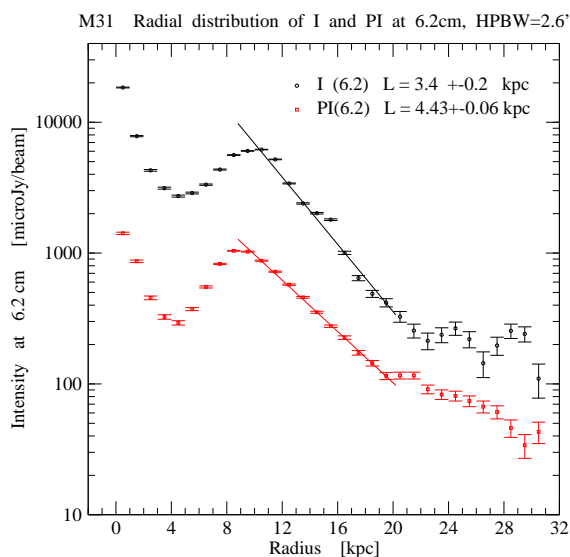


Fig. 16. Radial variations of total intensity *I* (black) and polarized intensity *PI* (red) at $\lambda 6.2$ cm at 2.6 HPBW, derived from the full extent of the observed area. This map is complete out to $R = 18$ kpc (or $80'$) along the minor axis. The exponential fits were restricted to the radial range between 9 kpc and 20 kpc. The scale lengths L are given in the figure.

The radial variations of *I*, *NTH*, *TH*, and *PI* at $\lambda 6.2$ cm at $3'$ HPBW are shown in Figure 17. For the range $R = 0 - 7$ kpc, we used the inclinations of the H I gas increasing from 31° at $R < 2$ kpc to 72° at $R = 6 - 7$ kpc as determined by Chemin et al. (2009), assuming that the same holds for the radio continuum emission. A close correspondence between gas and radio continuum features was first pointed out by Beck (1982) and Berkhuijsen et al. (1993) and is clearly visible in Figure 8 of Nieten et al. (2006). At larger radii we used the inclination of 75° again, which is consistent with the inclination of H I in this area. For each component we calculated the radial scale length between $R = 11$ kpc and $R = 15$ kpc, as shown in Figure 17 and listed in Table 4. With $L = (3.66 \pm 0.10)$ kpc for *NTH* and $L = (1.87 \pm 0.05)$ kpc for *TH*, the *NTH* emission clearly decreases much more slowly than the *TH* emission, indicating

M31 Radial distributions at 6.2cm for variable inclination

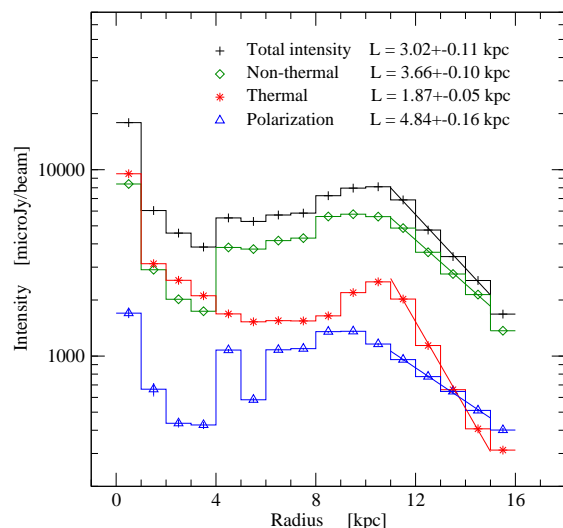


Fig. 17. Radial variations of total intensity *I* (black), non-thermal intensity *NTH* (green), thermal intensity *TH* (red), and polarized intensity *PI* (blue) at $\lambda 6.2$ cm at $3'$ HPBW. The exponential fits were restricted to the radial range between 11 kpc and 15 kpc. The scale lengths L are given in the figure.

propagation of the CREs away from their birth places in the star-forming regions. The scale length of *PI* of $L = (4.84 \pm 0.16)$ kpc is even larger than that of *NTH*, reflecting the large scale of the ordered magnetic field without influence of the turbulent fields of smaller scale that dominate the *NTH* emission.

Since propagation of CREs depends on frequency, we also calculated the scale lengths at $\lambda 20.5$ cm and $\lambda 3.6$ cm at the angular resolution of $3'$ and at the resolution of 1.5 . As before, we determined the scale lengths between 11 kpc and 15 kpc. All scale length results are given in Table 4.

Comparing the scale lengths at the resolution of $3'$, we see a clear decrease in L of *I* and *NTH* with increasing frequency: L for *NTH* drops from (4.08 ± 0.13) kpc at $\lambda 20.5$ cm to (2.79 ± 0.06) kpc at $\lambda 3.6$ cm. This reflects the decrease in the propagation length of the CREs with increasing frequency and makes *NTH* maps at $\lambda 20.5$ cm look smoother than those at $\lambda 3.6$ cm. In addition, the scale length of *PI* decreases between $\lambda 6.2$ cm and $\lambda 3.6$ cm, but not as strongly as that of *NTH*, because *PI* depends on the large-scale ordered magnetic field and *NTH* on both the ordered and the small-scale turbulent field. Naturally, the scale length of *TH* is the same at each frequency.

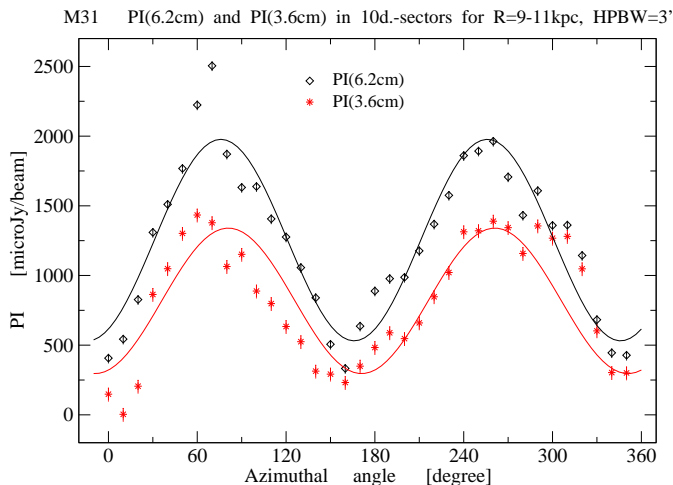
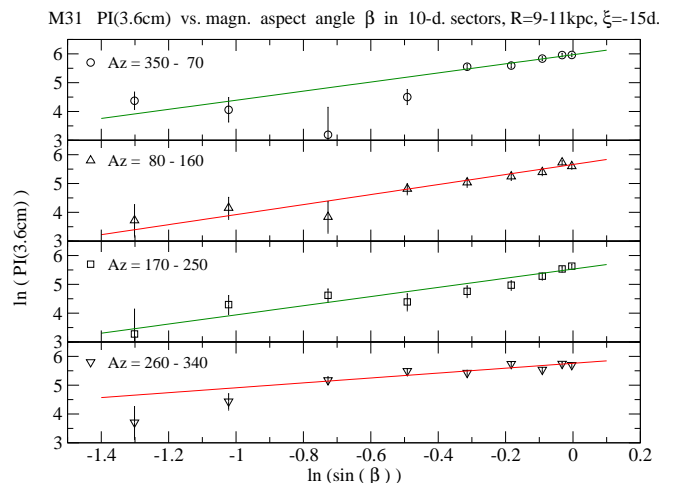
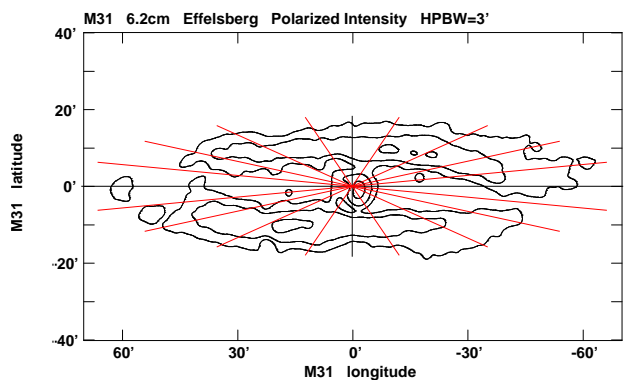
At the resolution of 1.5 the scale lengths of *I* and *NTH* at $\lambda 20.5$ cm are again larger than those at $\lambda 3.6$ cm by nearly the same amount as at $3'$ resolution. However, the scale lengths of *I* and *NTH* at 1.5 are significantly smaller than those at $3'$. Although at $\lambda 3.6$ cm the errors are quite large, the same trend is visible and is clearest for the scale length of *PI*. The scale lengths are larger at $3'$ resolution than at 1.5 resolution, because of the greater smoothing of the emission at $3'$ resolution than at 1.5 resolution. At $\lambda 3.6$ cm the effect is smaller than at $\lambda 20.5$ cm because the propagation length at the higher frequency is smaller than at $\lambda 20.5$ cm. As *TH* emission is least diffuse, at both frequencies the scale length of *TH* is only slightly smaller at 1.5 than at $3'$.

6. Azimuthal variation of polarized intensity

Polarized intensity *PI* is proportional to the component of the ordered (i.e. regular plus anisotropic turbulent) field perpendicu-

Table 4. Exponential scale lengths L for the radial range 11–15 kpc at three frequencies for total intensity I , non-thermal intensity NTH , polarized intensity PI , and thermal intensity TH .

Resolution [']	Component	L (λ 20.5 cm) [kpc]	L (λ 6.2 cm) [kpc]	L (λ 3.6 cm) [kpc]
3	I	3.66 ± 0.05	3.02 ± 0.11	2.46 ± 0.14
3	NTH	4.08 ± 0.13	3.66 ± 0.10	2.79 ± 0.06
3	PI	–	4.84 ± 0.16	3.79 ± 0.18
3	TH	1.90 ± 0.05	1.87 ± 0.05	1.87 ± 0.05
1.5	I	3.26 ± 0.14	–	2.35 ± 0.34
1.5	NTH	3.60 ± 0.09	–	2.72 ± 0.44
1.5	PI	–	–	3.00 ± 0.25
1.5	TH	1.69 ± 0.15	–	1.69 ± 0.15


Fig. 18. Variation of polarized intensity PI at λ 3.6 cm (red) and λ 6.2 cm (black) at 3' HPBW with azimuthal angle ϕ in the plane of M 31, averaged in 10° sectors in the ring between 9 kpc and 11 kpc radius. The azimuthal angle is counted anticlockwise from the north-eastern major axis of the ring in the plane of the sky (see Fig. 19). The lines show the weighted fits.

Fig. 20. Variation of polarized intensity PI at λ 3.6 cm (in μ Jy/beam, in \log_e scale) at 1.5 HPBW in four quadrants of M 31 with aspect angle $\sin\beta_{\text{ord}}$ (in \log_e scale) of the line of sight towards a spiral field with a pitch angle of $\xi_{\text{ord}} = -15^\circ$ for the radial ring between 9 kpc and 11 kpc. The lines show weighted fits through the data points. The fit results are given in Table 5.

Fig. 19. Sectors of 20° in width in the galaxy plane (red lines) and major and minor axes (black lines), superimposed onto contours of polarized intensity PI at λ 6.2 cm at 3' HPBW. Contour levels are at $(0.6, 1.2, 2.4) \times 1$ mJy/beam. The azimuthal angle is counted anticlockwise from the north-eastern major axis of the ring (left side).

lar to the line of sight, $B_{\text{ord},\perp}$. The strength of the PI depends on the strength and geometry of the ordered field, the density of the CREs, and the amount of depolarization.

Figure 18 shows the azimuthal variation of polarized intensity at λ 3.6 cm and λ 6.2 cm in the emission ring. Polarized intensity reveals maxima near the minor axis and minima near the major axis. Fits of a double-periodic curve give phase shifts of $-9^\circ \pm 3^\circ$ at λ 3.6 cm and $-14^\circ \pm 2^\circ$ at λ 6.2 cm, with the latter fit being statistically better. Variations in the CRE density or the strength of the ordered field are independent of the locations of the major and minor axis and cannot explain the variation seen in Fig. 18. Depolarization by Faraday dispersion in turbulent magnetic fields could in principle increase from the minor to the major axis due to the increasing path length through the emission ring. However, the emission ring between 9 kpc and 11 kpc radius is flat, with a scale height of the thermal gas of only about 0.5 kpc (Fletcher et al. 2004) compared to a radial width of about 4 kpc (Fig. 17), resulting in an almost constant path length between the minor and the major axis, which disfavors a strong variation in Faraday depolarization. Depolarization by RM gradients (Fletcher et al. 2004) is strongest near the minor axis (Fig. 24) and also cannot explain the variation in Fig. 18. Furthermore, Faraday depolarization is strongly wavelength dependent and is expected to be weak at λ 3.6 cm and λ 6.2 cm. In the next paper, we will discuss Faraday depolarization in detail.

We conclude that the variation in polarized intensity is due to variation in the orientation of the ordered field with respect to

Table 5. Results of the fitted lines shown in Fig. 20 for the four quadrants of the radial ring between 9 kpc and 11 kpc. The first column gives the range of azimuthal angle, the second the slope and its error, and the third the χ^2 value.

Azimuth [°]	Slope	χ^2
350 – 70	1.58 ± 0.25	1.8
80 – 160	1.74 ± 0.22	1.0
170 – 250	1.59 ± 0.27	1.6
260 – 340	0.85 ± 0.20	2.0

the line of sight. The polarized intensity is strongest around the minor axis and weakest around the major axis, which indicates that the orientation of the ordered field approximately follows the ring, as is clearly visible in Figs. 4 and 8, so that its component in the plane of the sky varies with azimuthal angle with a phase shift that is related to the spiral pitch angle ξ_{ord} of the large-scale ordered field.

To investigate this geometrical effect in detail, we computed the aspect angle β_{ord} between the ordered magnetic field and the line of sight, so that $B_{\text{ord},\perp} = B_{\text{ord}} \sin \beta_{\text{ord}}$ and $B_{\text{ord},\parallel} = B_{\text{ord}} \cos \beta_{\text{ord}}$. For a large-scale ASS pattern of the ordered field with a constant pitch angle ξ_{ord} ,

$$\cos \beta_{\text{ord}} = \cos(\phi - \xi_{\text{ord}}) \sin i, \quad (1)$$

where $i = 75^\circ$ is the galaxy inclination, and ϕ is the azimuthal angle in the galaxy plane, counted anticlockwise, with $\phi = 0^\circ$ on the north-eastern and $\phi = 180^\circ$ on the south-western major axis of the ring (see Fig. 19). For a constant CRE density, constant strength of the ordered field, constant path length through the emitting ring, and negligible Faraday depolarization, polarized intensity PI varies as

$$PI \propto N_{\text{CRE}} B_{\text{ord},\perp}^{1+\alpha_{\text{nth}}} \propto |(\sin \beta_{\text{ord}})^{1+\alpha_{\text{nth}}}|, \quad (2)$$

where α_{nth} is the synchrotron spectral index.² According to Eq. 2, the maxima of PI are expected at $\beta_{\text{ord}} = 90^\circ$ (i.e. at azimuthal angles of $\phi = (90^\circ + \xi_{\text{ord}})$ and $\phi = (270^\circ + \xi_{\text{ord}})$), and the minima at $\beta_{\text{ord}} = (90^\circ - i)$ (i.e. at $\phi = +\xi_{\text{ord}}$ and $\phi = (180^\circ + \xi_{\text{ord}})$).

When plotting $\log_e(PI)$ against $\log_e(\sin \beta_{\text{ord}})$, the slope of the fit should give $1 + \alpha_{\text{nth}}$ in the case of a perfect ASS field and no depolarization. Table 5 shows the results for four quadrants of the radial ring between 9 kpc and 11 kpc, each covering a range of azimuthal angles corresponding to a range in aspect angle between $\beta_{\text{ord}} = (90^\circ - i)$ and $\beta_{\text{ord}} = 90^\circ$. Here we assumed that the ordered field has a large-scale ASS pattern with a pitch angle of $\xi_{\text{ord}} = -15^\circ$.³ The slopes of the first three quadrants are consistent with the mean synchrotron spectral index of about 0.75 (Fig. 15). In these quadrants, the variation of PI is mostly due to the variation in aspect angle β . In the fourth quadrant (north) ($\phi = 260^\circ - 340^\circ$) the slope is significantly different from the expectation for the simple geometry. In this region the ordered field deviates from the assumed ASS geometry in strength and/or in orientation.

In a similar study by Beck (1982) of PI at $\lambda 11.1$ cm (Fig. 6 therein), the slopes were different from the expected value in all

² Eq. 2 is also valid for the case of equipartition between the energy densities of cosmic rays and total magnetic fields ($N_{\text{CRE}} \propto N_{\text{CR}} \propto B_{\text{tot}}^2$) because B_{tot} is dominated by small-scale turbulent fields that do not depend on β_{ord} .

³ While the fit to the $\lambda 6.2$ cm data in Fig. 18 gave $\xi_{\text{ord}} = -14^\circ \pm 2^\circ$, we decided to use a value of -15° , which gives a symmetric assignment of the azimuthal sectors to the four quadrants.

four quadrants, probably due to the lower resolution and significant Faraday depolarisation at that wavelength. Our new results are more consistent with the ASS field pattern.

Beck (1982) suggested that the field orientation follows gaseous spiral arms observed in H I (Unwin 1980a,b; Braun 1990; Chemin et al. 2009) that deviate from a simple ring structure. The main H I spiral arm in the north-western quadrant is almost straight from the minor axis to close to the major axis, so that β hardly varies, which may explain the small slope in Fig. 20 (bottom panel).

7. Faraday rotation and large-scale field pattern

Faraday rotation is a tool used to study the pattern of the large-scale regular field, but it is insensitive to a large-scale pattern of the anisotropic turbulent field. We computed Faraday rotation measures $RM = \Delta\chi/(\lambda_1^2 - \lambda_2^2)$ (where λ is measured in metres) from the polarization angles χ between $\lambda_1 = 0.1133$ m and $\lambda_2 = 0.0618$ m at $5'$ resolution, and also between $\lambda_1 = 0.0618$ m and $\lambda_2 = 0.0359$ m at $3'$ resolution (Figures 21 and 22). In both figures RM varies smoothly along the ring, with the lowest values near the north-eastern major axis and the highest near the south-western major axis. A few regions outside of the ring (near the left edge of Fig. 21) show significant deviations from this behaviour.

The RM s in the central region are different in the two figures: about -150 rad m⁻² in Fig. 21 and about -100 rad m⁻² in Fig. 22. Gießbübel & Beck (2014) measured the RM between $\lambda 6.2$ cm and $\lambda 3.5$ cm in the central region with $15''$ resolution and found periodic variations of about ± 100 rad m⁻² around the foreground $RM_{\text{fg}} \approx -100$ rad m⁻², which indicates a separate ASS field in the central region. The beam width of our new observations is too large to resolve this inner field.

If the large-scale ASS pattern of the ordered field found in Sect. 6 is also valid for the regular field (which is part of the ordered field), the RM is expected to vary as (see Krause et al. 1989)

$$RM = RM_{\text{fg}} + RM_{\text{max,a}} \cos \beta_{\text{reg}} = RM_{\text{fg}} + RM_{\text{max,a}} \cos(\phi - \xi_{\text{reg}}) \sin i, \quad (3)$$

where RM_{fg} is the RM contribution from the Milky Way in the foreground of M 31; ϕ is the azimuthal angle in the galaxy plane; β_{reg} is the aspect angle between the regular field and the line of sight; ξ_{reg} is the pitch angle of the regular field, assumed to be constant along ϕ ; and $RM_{\text{max,a}}$ is the maximum RM of the ASS mode near the south-western major axis of the ring (i.e. at the azimuthal angle $\phi = 180^\circ + \xi_{\text{reg}}$). Figures 23 and 24 show that sinusoidal variations give good fits to the data averaged in sectors of the radial ring between 9 kpc and 11 kpc.

The foreground RM s of the sinusoidal fits in the radial ring 9–11 kpc are similar, $RM_{\text{fg}} = (-118 \pm 3)$ rad m⁻² between $\lambda 11.3$ cm and $\lambda 6.2$ cm (Fig. 23) and $RM_{\text{fg}} = (-125 \pm 4)$ rad m⁻² between $\lambda 6.2$ cm and $\lambda 3.6$ cm (Fig. 24, black curve). The amplitude $RM_{\text{max,a}} = (78 \pm 6)$ rad m⁻² between $\lambda 11.3$ cm and $\lambda 6.2$ cm is lower compared to $RM_{\text{max,a}} = (118 \pm 9)$ rad m⁻² between $\lambda 6.2$ cm and $\lambda 3.6$ cm in the same radial range by a factor of ≈ 1.5 . As this factor characterizes the relative amount of Faraday depolarization, M 31 is less transparent to polarized emission (partly ‘Faraday thick’) at $\lambda 11.3$ cm compared to $\lambda 6.2$ cm and $\lambda 3.6$ cm.

We performed sinusoidal fits according to Eq. 3 for the RM data between $\lambda 6.2$ cm and $\lambda 3.6$ cm for five radial rings between

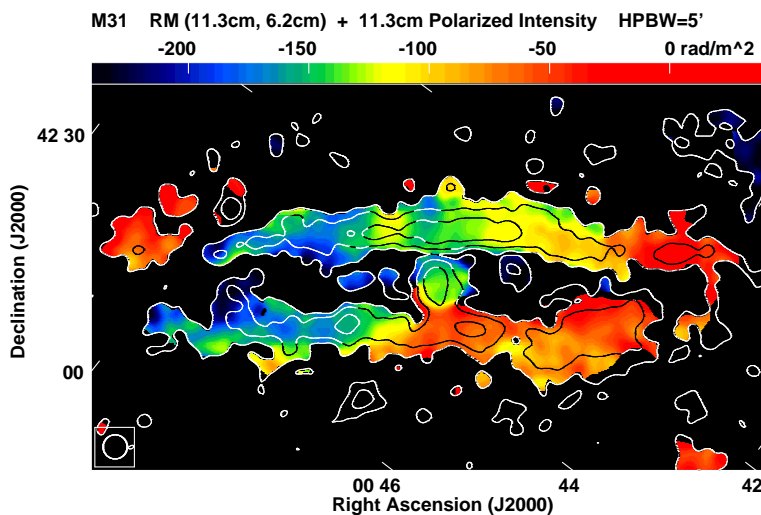


Fig. 21. Faraday rotation measure RM (colour) between $\lambda 11.3$ cm and $\lambda 6.2$ cm at $5'$ HPBW, calculated at pixels where PI at both frequencies exceeds three times the rms noise. The error decreases from 26 rad/m² at the lowest signal-to-noise ratio ($S/N = 3$) to about 3 rad/m² at the highest S/N . Contours show the polarized intensity at $\lambda 11.3$ cm at the same resolution. Contour levels are at 1 , 2 , and 4 mJy/beam. Polarized background sources have been subtracted. The HPBW is indicated in the bottom left corner. The coordinate system is rotated by -53° .

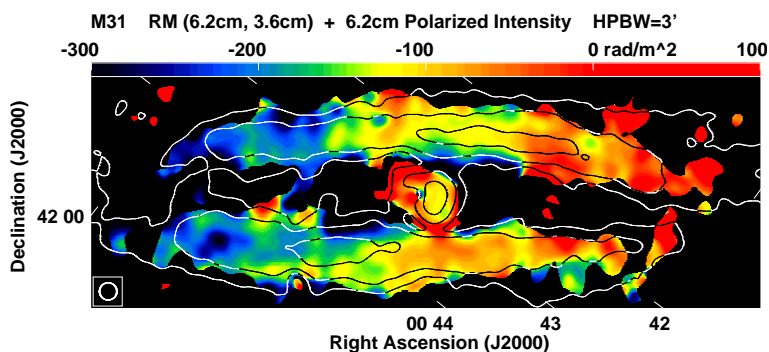


Fig. 22. Faraday rotation measure RM (colour) between $\lambda 6.2$ cm and $\lambda 3.6$ cm at $3'$ HPBW, calculated at pixels where PI at both frequencies exceeds three times the rms noise. The error decreases from 93 rad/m² at $S/N = 3$ to about 9 rad/m² at the highest S/N . Contours show the polarized intensity at $\lambda 6.2$ cm at the same resolution. Contour levels are at 0.5 , 1 , and 2 mJy/beam. Polarized background sources have been subtracted. The HPBW is indicated in the bottom left corner. The coordinate system is rotated by -53° .

Table 6. Fit results of the sinusoidal azimuthal variation of RM between $\lambda 6.2$ cm and $\lambda 3.6$ cm at $3'$ HPBW, averaged in sectors of 10° width, in five radial rings ΔR in the galaxy plane: foreground RM_{fg} ; amplitude $RM_{max,a}$; phase, corresponding to the average pitch angle ξ_{reg} of the regular field in the radial ring, and reduced χ^2 of the fit. The last column gives the average pitch angle ξ_{ord} of the ordered field, calculated from the B orientations, corrected for Faraday rotation, and averaged over all azimuthal angles of the radial ring. The uncertainty of ξ_{ord} is the error of the mean for the 36 sectors; the rms variation is about 6 times larger.

ΔR [kpc]	RM_{fg} [rad m ⁻²]	$RM_{max,a}$ [rad m ⁻²]	ξ_{reg} [$^\circ$]	χ^2	ξ_{ord} [$^\circ$]
7 – 8	-128 ± 7	93 ± 13	-4 ± 5	2.9	-30 ± 5
8 – 9	-118 ± 5	99 ± 10	-9 ± 3	2.3	-29 ± 4
9 – 10	-121 ± 5	120 ± 9	-7 ± 3	2.4	-26 ± 3
10 – 11	-130 ± 4	123 ± 8	-7 ± 2	1.1	-27 ± 2
11 – 12	-130 ± 6	129 ± 11	-5 ± 3	1.8	-27 ± 3

7 kpc and 12 kpc in the galaxy plane. The results are given in Table 6. The average RM_{fg} of (-125 ± 5) rad m⁻² is smaller than the values of about -90 rad m⁻² found based on previous data (Beck 1982; Berkhuijsen et al. 2003), but the new data are more reliable. The value of RM_{fg} does not show a significant variation with radius, indicating that RM s from the Milky Way do not vary on an angular scale similar to that of the ring width in

M 31. The amplitudes $RM_{max,a}$ increase with radius, indicating that the strength of the regular field of M 31 increases outwards, as already noted by Fletcher et al. (2004). The pitch angles ξ_{reg} are similar to the pitch angle of the gaseous spiral arms of about -7° (Arp 1964; Braun 1991; Chemin et al. 2009).

Linear models of α - Ω dynamo action in galaxies (Shukurov 2000) predict that the absolute value of the pitch angle $|\xi_{reg}|$ is

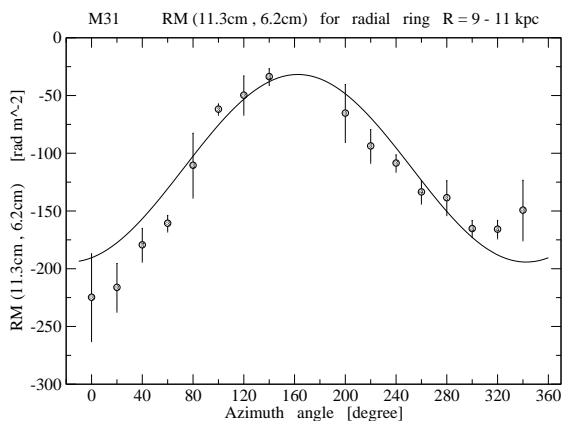


Fig. 23. Variation (with azimuthal angle in the galaxy plane) of Faraday rotation measures RM between $\lambda 11.3$ cm and $\lambda 6.2$ cm at $5'$ HPBW, averaged in the radial ring between 9 kpc and 11 kpc in sectors of 20° width, and the fitted sinusoidal line. The azimuthal angle is counted from the north-eastern major axis (left side in Fig. 21). The reduced χ^2 value is 4.0.

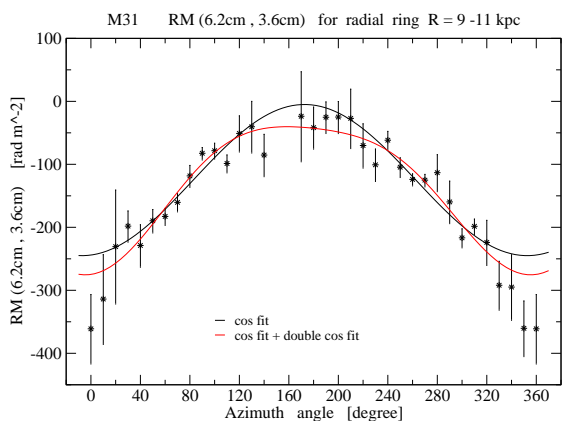


Fig. 24. Variation (with azimuthal angle in the galaxy plane) of Faraday rotation measures RM between $\lambda 6.2$ cm and $\lambda 3.6$ cm at $3'$ HPBW, averaged in the radial ring between 9 kpc and 11 kpc, in sectors of 10° width. The black line shows the sinusoidal fit, the red line the combined sinusoidal + double-periodic fit, with reduced χ^2 values of 1.3 for both fits.

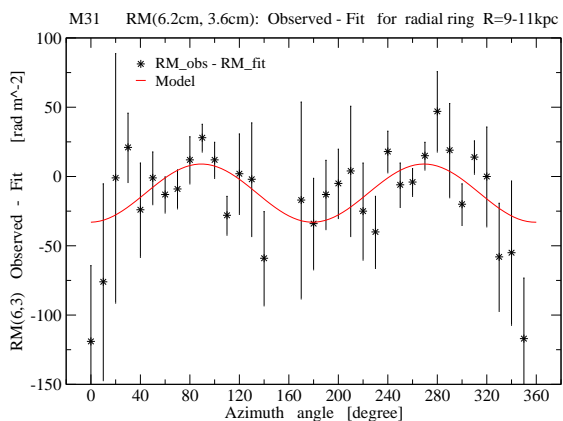


Fig. 25. Variation (with azimuthal angle in the galaxy plane) of the residual Faraday rotation measures RM between $\lambda 6.2$ cm and $\lambda 3.6$ cm at $3'$ HPBW, averaged in the radial ring between 9 kpc and 11 kpc, after subtracting the best-fitting sinusoidal model from Fig. 24 (black line). The reduced χ^2 value is 1.2.

constant for a flat rotation curve, but that it decreases with increasing radius if the scale height of the gas disc increases ('flaring disc'). According to the non-linear dynamo model developed by Chamandy & Taylor (2015), the magnetic pitch angle, in the saturated state of field evolution, depends on several parameters that may vary differently with radius. Our results (Table 6) indicate that ξ_{reg} is about constant with radius, consistent with the prediction from the simple model. On the other hand, the mode analysis of multi-frequency polarization angles used by Fletcher et al. (2004) yielded larger values of ξ_{reg} between -11° and -19° in radial rings similar to those in Table 6 and a hint of a radial decrease. However, anisotropic turbulent fields (which affect polarization angles and intensities but not RM s) are neglected in the method of Fletcher et al. (2004), so that their values of ξ_{reg} are correct only if $\xi_{\text{ord}} \approx \xi_{\text{reg}}$.

The azimuthal RM variation in Fig. 24 shows significant deviations from the sinusoidal fit (black curve). Sofue & Beck (1987) suggested the existence of a BSS mode superimposed onto the ASS mode. The azimuthal variation of RM for a BSS field is (Krause 1990)

$$RM = RM_{\text{fg}} + RM_{\text{max,b}} \cos(2\phi - \delta) \sin i, \quad (4)$$

where ϕ is the azimuthal angle in the galaxy plane and δ the phase, which is related to the pitch angle and the position angle of the spiral pattern in the galaxy plane.

The red curve in Fig. 24 shows the fit for the combined $ASS + BSS$ field, for the radial range 9–11 kpc where the signal-to-noise ratios are highest. The amplitude of the BSS field is $RM_{\text{max,b}} = (21 \pm 7) \text{ rad m}^{-2}$, about six times smaller than the amplitude $RM_{\text{max,a}}$ of the ASS mode. The fit of the combined modes is not statistically better because the BSS field is weak. We computed the residuals from the ASS fit (Fig. 25), which vary double-periodically with azimuthal angle and hence support the superimposed BSS field.

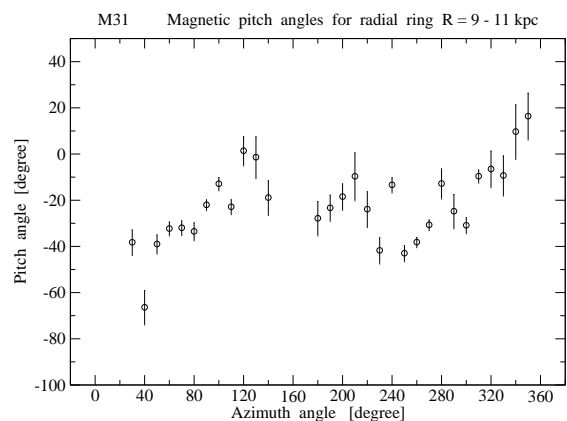


Fig. 26. Variation (with azimuthal angle in the galaxy plane) of the intrinsic pitch angle ξ_{ord} of the ordered magnetic field, calculated from the intrinsic orientations of the ordered field at $3'$ HPBW, corrected with RM s between $\lambda 6.2$ cm and $\lambda 3.6$ cm, and averaged in the radial ring between 9 kpc and 11 kpc.

Faraday rotation allows us to compute the intrinsic pitch angle ξ_{ord} of the ordered field from the observed orientation of the polarized emission in two steps, to be compared with ξ_{reg} as computed above. Firstly, the RM s shown in Figs. 21 or 22 were used to correct the orientation χ_{obs} of the ordered magnetic field in the plane of the sky observed at wavelength λ for Faraday rotation in order to achieve the intrinsic orientation (i.e. at infinitely small

wavelength) in the plane of the sky via $\chi_{\text{ord}} = \chi_{\text{obs}} - RM \lambda^2$. Then the intrinsic pitch angle ξ_{ord} of the ordered field in the galaxy plane follows from

$$\xi_{\text{ord}} = \phi + 90^\circ - \arctan[\tan(\chi_{\text{ord}} - \chi_p) / \cos i], \quad (5)$$

where χ_{ord} is the intrinsic position angle of the ordered field in the plane of the sky and χ_p is the position angle of the major axis of the galaxy in the plane of the sky.

The azimuthal variation of the intrinsic pitch angle ξ_{ord} in the ring 9–11 kpc, calculated from the intrinsic orientations of the ordered field at 3' resolution, corrected with RM_s between $\lambda 6.2$ cm and $\lambda 3.6$ cm, is shown in Figure 26. The average pitch angle is $-26^\circ \pm 3^\circ$ (weighted according to error bars). The average pitch angle derived from the intrinsic polarization angles at 5' resolution, corrected with RM_s between $\lambda 11.3$ cm and $\lambda 6.2$ cm, in the same radial range 9–11 kpc is $-17^\circ \pm 6^\circ$ (also weighted according to error bars), consistent with the value obtained using the smaller wavelengths. In order to search for any radial variation, we computed averages of ξ_{ord} in five radial rings, given in the last column of Table 6. No significant variation with radius is found.

The large variations in the intrinsic pitch angles ξ_{ord} seen in Fig. 26 indicate that the field structure is more complex than an $ASS + BSS$ field. The value of ξ_{ord} jumps by about 70° from positive to negative values near the north-eastern major axis ($\phi \approx 0^\circ$), and ξ_{ord} calculated from the intrinsic orientations of the ordered field, corrected with RM_s between $\lambda 11.3$ cm and $\lambda 6.2$ cm, shows a similar behaviour. We propose that ξ_{ord} is affected by local field deviations and/or anisotropic turbulent fields.

The averages of ξ_{ord} in Table 6 are significantly smaller than those of ξ_{reg} and the pitch angle of the gaseous spiral arms of about -7° . Pitch angles of the ordered field that deviate from those of the gaseous spiral arms have also been found in the spiral galaxies M 74 (Mulcahy et al. 2017), M 83 (Frick et al. 2016), and M 101 (Berkhuijsen et al. 2016). These results were believed to show that the mean-field dynamo does not generate regular fields that are aligned with the spiral arms because ξ_{reg} depends on several parameters that are unrelated to spiral arms (Chamandy & Taylor 2015).

The results for M 31 presented here suggest a different interpretation: B_{ord} has two components, the regular field B_{reg} and the anisotropic turbulent field B_{an} . As ξ_{reg} in Table 6 is similar to the pitch angle of the gaseous spiral arms of about -7° , the deviation may arise in the anisotropic turbulent field. The regular field B_{reg} and the anisotropic turbulent field B_{an} have different spiral patterns that may be shaped by different physical processes.

8. Summary and conclusions

In order to study the magnetic field structure of M 31, we used the Effelsberg telescope to perform three new deep radio continuum surveys in total intensity and polarization at the wavelengths of $\lambda 11.3$ cm (2.645 GHz), $\lambda 6.2$ cm (4.85 GHz), and $\lambda 3.6$ cm (8.35 GHz). The angular resolutions (HPBW) are 4'.4, 2'.6, and 1'.6, respectively (Table 2). As we wanted to study the large-scale emission, we subtracted point sources unrelated to M 31 at each wavelength. The resulting maps are shown in Figure 1 to Figure 10.

In this first paper we have presented the observations and reduction procedures and discussed results on the spectral index and radial scale lengths, and on Faraday rotation measures and pitch angles of the regular magnetic field. Below we summarize our main conclusions:

1. At all wavelengths the well-known emission ring between about 7 kpc and 13 kpc radius in the galaxy plane stands out, both in I and in PI. The nuclear region is also very bright. PI is low on the major axis of the ring in the plane of the sky on both sides, which is a first indication that the ordered magnetic field is oriented along the bright ring, so that the field component in the plane of the sky is smallest near the major axis.

2. Including all available surveys between 0.3 GHz and 4.85 GHz, covering M 31 to at least $R = 16$ kpc, we find a spectral index of the integrated total emission of $\alpha = 0.71 \pm 0.02$ (defined as $S \propto \nu^{-\alpha}$). After subtraction of the thermal emission, we obtain a spectral index of the integrated non-thermal emission of $\alpha_n = 0.81 \pm 0.03$.

3. The spectral indices vary across M 31. Maps of total and non-thermal spectral indices between $\lambda 21.1$ cm and $\lambda 3.6$ cm at 1'.5 resolution show that α (α_n) is about 0.4 (0.5) near star-forming regions and steepens to about 1.0 towards the inner and outer parts of the bright ring due to radiation losses of the CREs propagating away from their birth places near the star-forming regions.

4. The radial variation of the intensities of I, NTH, PI, and TH all peak between 8 and 12 kpc radius, but their scale lengths (L) differ. At $\lambda 6.2$ cm and 3' resolution, between $R = 11$ kpc and $R = 15$ kpc, we find $L(I) = (3.02 \pm 0.11)$ kpc, $L(NTH) = (3.66 \pm 0.10)$ kpc, $L(PI) = (4.84 \pm 0.16)$ kpc, and $L(TH) = (1.87 \pm 0.05)$ kpc. The longer scale lengths of NTH and PI than of TH again indicate energy losses of the CREs when travelling away from their birthplaces near star-forming regions. The difference in scale lengths shows that the propagation length of the CREs could be several kpc.

5. The polarized intensity, averaged in azimuthal sectors in the radial ring between 9 kpc and 11 kpc in the galaxy plane, varies with azimuthal angle as a double-periodic curve, with maxima near the minor axis and minima near the major axis. This indicates that the ordered magnetic field is oriented almost along the ring but has a small pitch angle.

6. Faraday rotation measures (RM_s) between $\lambda 11.3$ cm and $\lambda 6.2$ cm and between $\lambda 6.2$ cm and $\lambda 3.6$ cm, averaged in azimuthal sectors of the radial ring between 9 kpc and 11 kpc, vary smoothly along the emission ring as a cosine function with azimuthal angle in the galaxy plane, which is a signature of a regular field with an axisymmetric spiral (ASS) pattern. The phase shift of the variation of $-7^\circ \pm 2^\circ$ is interpreted as the average spiral pitch angle of the regular field. It shows no significant variation with radius and is similar to the pitch angle of the gaseous spiral arms.

7. The residuals between the RM_s computed between $\lambda 6.2$ cm and $\lambda 3.6$ cm and the ASS fit show a double-periodic variation with azimuthal angle, indicative of a superimposed BSS mode of the regular field, with an about six times smaller amplitude compared to the ASS mode.

8. The amplitude of the RM_s between $\lambda 11.3$ cm and $\lambda 6.2$ cm between 9 kpc and 11 kpc radius is about 1.5 times lower than between $\lambda 6.2$ cm and $\lambda 3.6$ cm, indicating that Faraday depolarization at $\lambda 11.3$ cm is stronger (greater Faraday thickness) than at $\lambda 6.2$ cm and $\lambda 3.6$ cm).

9. The average pitch angle of the ordered field, derived from the intrinsic orientations of the polarized emission between 9 kpc and 11 kpc radius, is $-26^\circ \pm 3^\circ$. The difference in pitch angles of regular and ordered field indicates that the ordered field contains a significant fraction of an anisotropic turbulent field that has a pattern that is different to the regular ($ASS + BSS$) field.

New insights to the magnetic field of M 31, especially measuring the extent in the outer disc and the search for large-scale reversals, can be expected from deep observations of polarized background sources in L band ($\lambda 20$ cm, hence improving the pioneering work performed by Han et al. (1998)). While the southern location of the Square Kilometre Array (SKA, under construction) hampers observation of M 31, the Jansky Very Large Array (JVLA) and APERTIF (Oosterloo et al. 2018) are suitable instruments for such investigations.

Acknowledgements. We thank the operators at the Effelsberg telescope for support during on-site observations and for supervising remote observations. We thank Patricia Reich for her support at various stages of data processing, especially for writing the turboplat script and for an early version of the script subtrans. Peter Müller is acknowledged for making several data processing scripts available to us already during the development of NOD3. We thank Marita Krause, Andrew Fletcher, and the anonymous referee for careful reading of the manuscript and useful suggestions.

References

- Arp, H. 1964, *ApJ*, 139, 1045
- Arshakian, T. G. & Beck, R. 2011, *MNRAS*, 418, 2336
- Arshakian, T. G., Beck, R., Krause, M., & Sokoloff, D. 2009, *A&A*, 494, 21
- Beck, R. 1982, *A&A*, 106, 121
- Beck, R. 2007, *A&A*, 470, 539
- Beck, R. 2015, *A&A Rev.*, 24, 4
- Beck, R., Berkhuijsen, E. M., & Hoernes, P. 1998, *A&AS*, 129, 329
- Beck, R., Berkhuijsen, E. M., & Wielebinski, R. 1980, *Nature*, 283, 272
- Beck, R., Brandenburg, A., Moss, D., Shukurov, A., & Sokoloff, D. 1996, *ARA&A*, 34, 155
- Beck, R. & Golla, G. 1988, *A&A*, 191, L9
- Beck, R. & Gräve, R. 1982, *A&A*, 105, 192
- Beck, R., Loiseau, N., Hummel, E., et al. 1989, *A&A*, 222, 58
- Berkhuijsen, E. M. 1977, *A&A*, 57, 9
- Berkhuijsen, E. M., Bajaja, E., & Beck, R. 1993, *A&A*, 279, 359
- Berkhuijsen, E. M., Beck, R., & Hoernes, P. 2003, *A&A*, 398, 937
- Berkhuijsen, E. M., Beck, R., & Tabatabaei, F. S. 2013, *MNRAS*, 435, 1598
- Berkhuijsen, E. M., Urbanik, M., Beck, R., & Han, J. L. 2016, *A&A*, 588, A114
- Berkhuijsen, E. M., Wielebinski, R., & Beck, R. 1983, *A&A*, 117, 141
- Boulares, A. & Cox, D. P. 1990, *ApJ*, 365, 544
- Brandenburg, A. & Subramanian, K. 2005, *Phys. Rep.*, 417, 1
- Braun, R. 1990, *ApJS*, 72, 755
- Braun, R. 1991, *ApJ*, 372, 54
- Braun, R., Thilker, D. A., Walterbos, R. A. M., & Corbelli, E. 2009, *ApJ*, 695, 937
- Brinks, E. & Shane, W. W. 1984, *A&AS*, 55, 179
- Chamandy, L. 2016, *MNRAS*, 462, 4402
- Chamandy, L. & Taylor, A. R. 2015, *ApJ*, 808, 28
- Chemin, L., Carignan, C., & Foster, T. 2009, *ApJ*, 705, 1395
- de Vaucouleurs, G., de Vaucouleurs, A., & Corwin, J. R. 1976, in *Second reference catalogue of bright galaxies*, Vol. 1976, p. Austin: University of Texas Press., Vol. 1976
- Devereux, N. A., Price, R., Wells, L. A., & Duric, N. 1994, *AJ*, 108, 1667
- Emerson, D. T. & Gräve, R. 1988, *A&A*, 190, 353
- Emerson, D. T., Klein, U., & Haslam, C. G. T. 1979, *A&A*, 76, 92
- Evirgen, C. C., Gent, F. A., Shukurov, A., Fletcher, A., & Bushby, P. J. 2019, *MNRAS*, 488, 5065
- Fletcher, A., Berkhuijsen, E. M., Beck, R., & Shukurov, A. 2004, *A&A*, 414, 53
- Frick, P., Stepanov, R., Beck, R., et al. 2016, *A&A*, 585, A21
- Fritz, J., Gentile, G., Smith, M. W. L., et al. 2012, *A&A*, 546, A34
- Gießübel, R. 2012, PhD dissertation, Universität zu Köln, Cuvillier Verlag Göttingen, ISBN 978-3-95404-308-8
- Gießübel, R. & Beck, R. 2014, *A&A*, 571, A61
- Gießübel, R., Heald, G., Beck, R., & Arshakian, T. G. 2013, *A&A*, 559, A27
- Golla, G. 1989, Diploma thesis, Universität zu Bonn
- Gordon, K. D., Bailin, J., Engelbracht, C. W., et al. 2006, *ApJ*, 638, L87
- Han, J. L., Beck, R., & Berkhuijsen, E. M. 1998, *A&A*, 335, 1117
- Hanasz, M., Wóltański, D., & Kowalik, K. 2009, *ApJ*, 706, L155
- Haverkorn, M., Katgert, P., & de Bruyn, A. G. 2003, *A&A*, 403, 1045
- Hoernes, P., Berkhuijsen, E. M., & Xu, C. 1998, *A&A*, 334, 57
- Iacobelli, M., Haverkorn, M., & Katgert, P. 2013, *A&A*, 549, A56
- Jacoby, G. H., Ford, H., & Ciardullo, R. 1985, *ApJ*, 290, 136
- Jelić, V., de Bruyn, A. G., Pandey, V. N., et al. 2015, *A&A*, 583, A137
- Kothes, R., Reich, P., Foster, T. J., & Reich, W. 2017, *A&A*, 597, A116
- Krause, M. 1990, in *IAU Symposium*, Vol. 140, Galactic and Intergalactic Magnetic Fields, ed. R. Beck, R. Wielebinski, & P. P. Kronberg, 187–196
- Krause, M., Hummel, E., & Beck, R. 1989, *A&A*, 217, 4
- Krumholz, M. R. & Federrath, C. 2019, *Frontiers in Astronomy and Space Sciences*, 6, 7
- Melchior, A.-L. & Combes, F. 2011, *A&A*, 536, A52
- Moss, D., Stepanov, R., Arshakian, T. G., et al. 2012, *A&A*, 537, A68
- Mulcahy, D. D. 2011, Master thesis, Universität zu Bonn
- Mulcahy, D. D., Beck, R., & Heald, G. H. 2017, *A&A*, 600, A6
- Müller, P., Beck, R., & Krause, M. 2017a, *A&A*, 600, A63
- Müller, P., Krause, M., Beck, R., & Schmidt, P. 2017b, *A&A*, 606, A41
- Nieten, C., Neiningner, N., Guélin, M., et al. 2006, *A&A*, 453, 459
- Oosterloo, T., van Leeuwen, J., Van Cappellen, W., Kruihof, G., & Jackson, C. 2018, in *Westerbork Telescope 50th Anniversary*, Vol. 361, 16
- Peng, B., Kraus, A., Krichbaum, T. P., & Witzel, A. 2000, *A&AS*, 145, 1
- Perley, R. A. & Butler, B. J. 2013, *ApJS*, 206, 16
- Perley, R. A. & Taylor, G. B. 2003, *NRAO Tech. Rep.*
- Rahmani, S., Lianou, S., & Barmby, P. 2016, *MNRAS*, 456, 4128
- Ruzmaikin, A., Sokolov, D., Shukurov, A., & Beck, R. 1990, *A&A*, 230, 284
- Ruzmaikin, A. A., Sokolov, D. D., & Shukurov, A. M., eds. 1988, *Astrophysics and Space Science Library*, Vol. 133, Magnetic fields of galaxies

- Schnitzeler, D. H. F. M., Katgert, P., & de Bruyn, A. G. 2009, *A&A*, 494, 611
- Shukurov, A. 2000, in *Proceedings 232. WE-Heraeus Seminar*, ed. E. M. Berkhuijsen, R. Beck, & R. A. M. Walterbos, 191–200
- Sieber, W., Haslam, C. G. T., & Salter, C. J. 1979, *A&A*, 74, 361
- Sofue, Y. & Beck, R. 1987, *PASJ*, 39, 541
- Sofue, Y. & Takano, T. 1981, *PASJ*, 33, 47
- Sokoloff, D. D., Bykov, A. A., Shukurov, A., et al. 1998, *MNRAS*, 299, 189
- Stanek, K. Z. & Garnavich, P. M. 1998, *ApJ*, 503, L131
- Stepanov, R., Arshakian, T. G., Beck, R., Frick, P., & Krause, M. 2008, *A&A*, 480, 45
- Tabatabaei, F. S. & Berkhuijsen, E. M. 2010, *A&A*, 517, A77
- Tabatabaei, F. S., Berkhuijsen, E. M., Frick, P., Beck, R., & Schinnerer, E. 2013a, *A&A*, 557, A129
- Tabatabaei, F. S., Schinnerer, E., Murphy, E. J., et al. 2013b, *A&A*, 552, A19
- Unwin, S. C. 1980a, *MNRAS*, 190, 551
- Unwin, S. C. 1980b, *MNRAS*, 192, 243
- Van Eck, C. L., Haverkorn, M., Alves, M. I. R., et al. 2017, *A&A*, 597, A98
- Zweibel, E. G. 2013, *Physics of Plasmas*, 20, 055501